Analysis of Joint Shape Variation from Multi-Object Complexes

Zhiyuan Liu[1] · Jörn Schulz[2] · Mohsen Taheri[2] · Martin Styner[1] · James Damon[3] · Stephen Pizer[1] · J. S. Marron[4]

Abstract

Shape correlation of multi-object complexes in the human body can have significant implications in understanding the development of disease. While there exist geometric and statistical methods that aim for multi-object shape analysis, very little research can effectively extract shape correlation. It is especially difficult to extract the correlation when the involved objects have different variability in separate non-Euclidean spaces. To address these difficulties, this paper proposes geometric and statistical methods to extract the shape correlation from multi-object complexes. In particular, we focus on the shape correlation of the hippocampus and the caudate subject to the development of autism. The proposed methods are designed (1) to capture objects' shape features (2) to capture shape correlation regardless of different variability between the two objects and (3) to provide interpretable shape correlation in multi-object complexes. In our experiments on synthetic data and autism data, the quantitative results and the qualitative visualization suggest that our methods are effective and robust.

Keywords Multi-object shape analysis · Shape correlation · Joint shape variation · Autism classification

1 Introduction

Structures in the human body are often functionally and spatially interrelated. The shape correlation between these related structures should be closely associated with the bio-logical variation (e.g., disease). Also, multi-object complexes contain information additional to the information in single-object complexes. This additional information is expected to be useful in understanding the biological variation.

For example, previous research on the development of Autism Spectrum Disorder (ASD) has found association with the shape of single brain structures (see e.g., [10,25,35,36]), including the hippocampus and the caudate. However, this research has not effectively revealed the joint shape variation[1] of the related structures subject to the development of ASD. The difficulties of analyzing the joint shape variation come from many directions. First, because the shape correlation is often coupled with variation of relative pose and size of multiple objects, it is difficult to extract the shape correlation [14]. Second, it is difficult to obtain robust patterns of shape correlations because of different variability across multiple objects and also because of the complex data space. Third, it is often difficult to interpret the shape correlation, making the results hypothetical to researchers and clinical users.

Many existing geometric and statistical methods attempt to address the above difficulties (see e.g., [4,29,34]). For instance, deformation-based methods (e.g., [16]) analyze the deformation of multi-object complexes involving the

✉ Zhiyuan Liu
  zhiy@cs.unc.edu

  Jörn Schulz
  jorn.schulz@uis.no

  Mohsen Taheri
  mohsen.taherishalmani@uis.no

  Martin Styner
  styner@cs.unc.edu

  James Damon
  jndamon@email.unc.edu

  Stephen Pizer
  pizer@cs.unc.edu

  J. S. Marron
  marron@unc.ed

1   Department of Computer Science, University of North Carolina at Chapel Hill (UNC), Chapel Hill, USA

2   Department of Mathematics & Physics, University of Stavanger (UiS), Stavanger, Norway

3   Department of Mathematics, UNC, Chapel Hill, USA

4   Department of Statistics and Operations Research, UNC, Chapel Hill, USA

---

[1] In this paper, "joint shape variation" is used interchangeably with "shape correlation".

ambient space. However, the principal variation can be biased by the variation of relative pose between objects. Statistical methods (e.g., [32,44,47]) of multi-block data analysis show promise in extracting correlation in multi-object complexes. Nonetheless, few such statistical methods can effectively extract correlation of shape data due to the complex data space, as discussed in Sect. 6.

In this paper, we extend geometric and statistical methods to extract joint shape variation in two-object complexes. We use boundary points derived from skeletal representations (s-reps [37]) to capture shape features. Then we extract joint shape variation from two blocks of shape features via our method called Non-EUclidean Joint and Individual Variation Explained (NEUJIVE). The resulting jointly varying features are the basis of hypothesis testing and classification. Because previous research has shown significant association between the development of ASD and shape features of either the hippocampus or the caudate [17], we verify the joint shape variation of the hippocampus-caudate pairs using our methods in classification of the ASD versus non-ASD group.

NEUJIVE is designed for extracting robust joint shape variation from multi-object complexes where the variability across multiple objects can be largely different. In essence, NEUJIVE is an extension of a recent method called Angle-based Joint and Individual Variation Explained (AJIVE) [12]. Different from AJIVE, our extension accounts for non-Euclidean properties of each object. Specifically, NEUJIVE consists of two critical steps: (1) convert shape descriptors to Euclidean representations and (2) extract the joint variation from the two-block Euclidean data via AJIVE. Considering the spherical property of shape data after removal of translation and scale [9], we adopt a method called Principal Nested Spheres (PNS) [24] to obtain the Euclidean representations for each object. By combining PNS and AJIVE, NEUJIVE can effectively extract joint shape variation that is insensitive to different variability of objects.

To capture shape features of objects with good correspondence, we adopt skeletally implied boundary points from s-reps. These implied boundary points capture smooth geometric features of individual objects for the joint analysis. Moreover, the s-rep implied boundary points allow straightforward interpretation of the joint shape variation.

We show the effectiveness and robustness of the above geometric and statistical methods in synthetic data and real shape data relating to ASD. Our key contributions in this paper can be summarized as below.

1. We propose a new statistical method for multi-object shape analysis, called NEUJIVE, to extract the joint shape variation from multi-object complexes. We have deliberately designed simulations to demonstrate the effectiveness and robustness of NEUJIVE in extracting joint variation from multi-block non-Euclidean data.

2. We propose analyzing joint shape variation from NEU-JIVE in real shape data relating to ASD. Because ASD is found to change the shape of multiple brain structures, the joint shape variation of multiple functionally related brain structures ought to have strong association with the development of ASD. The good interpretability of the joint shape variation can lead to interesting findings with respect to the development of ASD.

3. We propose using s-rep implied boundary points in the joint analysis of the hippocampus and the caudate. On the one hand, these implied boundary points provide smooth geometric features with good correspondence across a population. On the other hand, it is straightforward to interpret the results from NEUJIVE on the basis of the s-rep implied boundary points.

The rest of this paper is organized as follows. In Sect. 2 we introduce our driving problem and our solution that utilizes joint shape variation in classification. To produce the joint shape variation, in Sects. 3 to 5 we detail our methods that (1) capture shape features via s-rep implied boundary points (2) Euclideanize each block of shape features and (3) extract joint variation from two Euclidean blocks via AJIVE. Section 6 discusses relevant methods, with which we compare our method. In Sect. 7 we demonstrate that our proposed method can extract useful patterns from simulated two-block non-Euclidean data. Then we show another simulation to verify the benefit of the joint shape variation in classification. Last, our methods are verified in applications (including hypothesis testing and classification) to ASD data. Section 8 discusses a general form and broader impact of our methods. The paper concludes with remarks and discussions in Sect. 9. We introduce the source code that implements the methods and the simulated experiments in Sect. 10.

2 Classify ASD versus Non-ASD with Subcortical Shape

We want to take advantage of classification to demonstrate the effectiveness of NEUJIVE in extracting the joint shape variation from two-object complexes. An effective joint shape variation that has strong association with the development of ASD ought to improve classification performance. To this end, this section discusses the classification framework in which we use shape correlation in two-object complexes as classifying features.

To classify the ASD and the non-ASD group, we set up a binary classification model as
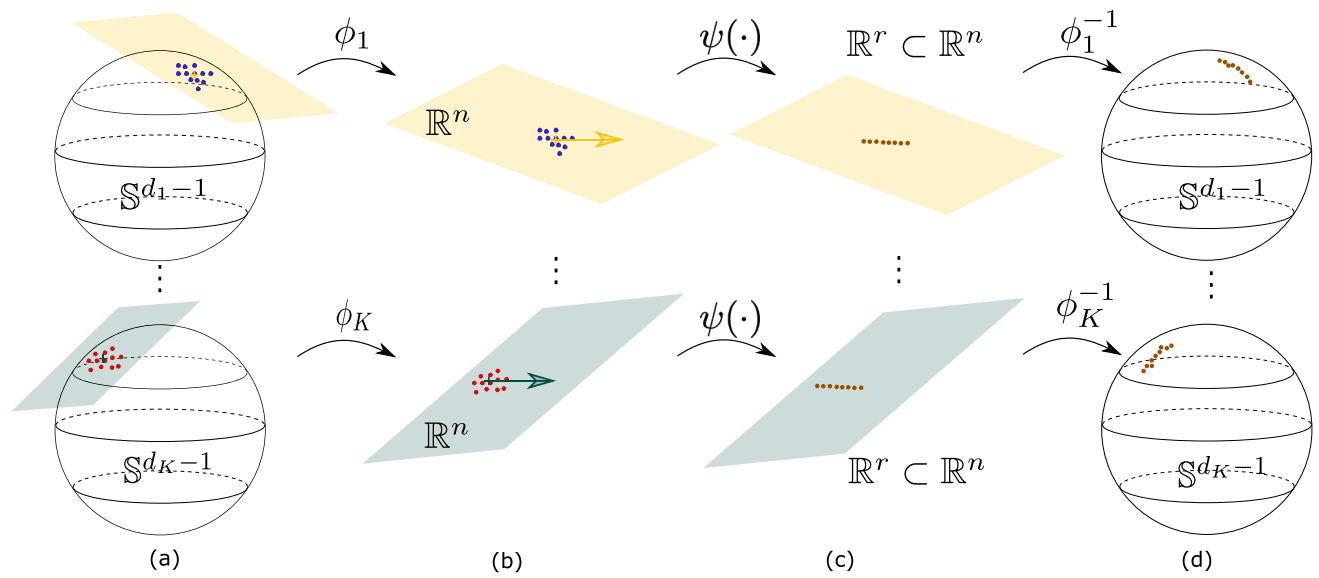
$$\hat{y} = \sigma(w^T X) \tag{1}$$

Fig. 1 The framework of extracting the joint components with NEU-JIVE. Column **a**: Input data live in K pre-shape spaces. Column **b**: Euclidean representations of the K blocks form the score space $\mathbb{R}^n$ (shown as the yellow and green planes), in which the joint variation subspaces (shown as the yellow and green arrows) live. Column **c**: Extract the joint components from the K blocks, yielding the joint structures (brown dots) that live in $\mathbb{R}^r$. Here, r denotes the dimension of the joint variation subspace. **d** For interpretation of the joint structures, we map the joint structures back to the pre-shape space via ϕ_k^{-1} for $k = \{1, \cdots, K\}$ (Color figure online)

where $w \in \mathbb{R}^{d \times 1}$ is a learnable weight vector, d is the dimension of the feature space and T means transpose. The matrix $X \in \mathbb{R}^{d \times n}$ represents the data of n configurations in our proposed feature space. We highlight that in this paper the rows of X are features, while the columns are cases. The output $\hat{y} \in \{0, 1\}^n$ denotes the vector of predicted labels for the n configurations. The symbol $\sigma(\cdot)$ denotes a mapping to the predicted binary class labels.

Our contributions concentrate on producing the feature matrix X that captures the joint shape variation of the hippocampus and the caudate. Because this joint shape variation should be strongly associated with the development of ASD [40,41], the use of the joint shape variation ought to produce good classification performance. We propose methods to extract the joint shape variation in an unsupervised way, making use of PNS and AJIVE, as illustrated in Fig. 1.

As we focus on two-object complexes (i.e., the hippocampus-caudate pairs), let $X_1 \in \mathbb{R}^{d_1 \times n}$ denote the shape descriptors of the hippocampi, where d_1 denotes the dimension of the feature vector of a hippocampus and n denotes the number of complexes. Likewise, let $X_2 \in \mathbb{R}^{d_2 \times n}$ denote the shape descriptors of the caudate nuclei, where d_2 denotes the dimension of the feature space of the caudate. In many cases, both d_1 and d_2 are larger than the number of samples n.

Our first step is to capture shape features of each single object. Next, because shape features should be invariant under translation and scaling, we map the geometric features onto a unit hypersphere. Then we obtain Euclidean representations of each object via PNS. Let ϕ denote the transformation from shape features to Euclidean representations of each object, i.e.,

$$\phi : \mathbb{R}^{d \times n} \mapsto \mathbb{R}^{(n-1) \times n} \tag{2}$$

where d is the dimension of the shape descriptors of the object and $d \gg n$. Because n data points lie in a hypersphere of dimension $n - 1$, higher level PNS components are not included.

Finally, we extract the joint shape variation from the two PNS blocks using AJIVE. We use ψ to denote the mapping from the two PNS blocks of Eq. (2) to the low dimensional joint variation space, i.e.,

$$\psi : \mathbb{R}^{(n-1) \times n} \times \mathbb{R}^{(n-1) \times n} \mapsto \mathbb{R}^{r \times n} \tag{3}$$

where r denotes the dimension of the joint variation space.

Essentially, our proposed joint shape variation is obtained by composing Euclideanization and the AJIVE, i.e.,

$$X = \psi(\phi(X_1), \phi(X_2)) \tag{4}$$

where X_1 and X_2 denote shape features of the two objects, respectively.

In the following, Sect. 3 discusses capturing the shape of the hippocampus and of the caudate, resulting in feature matrices X_1 and X_2. Section 4 details the transformation ϕ
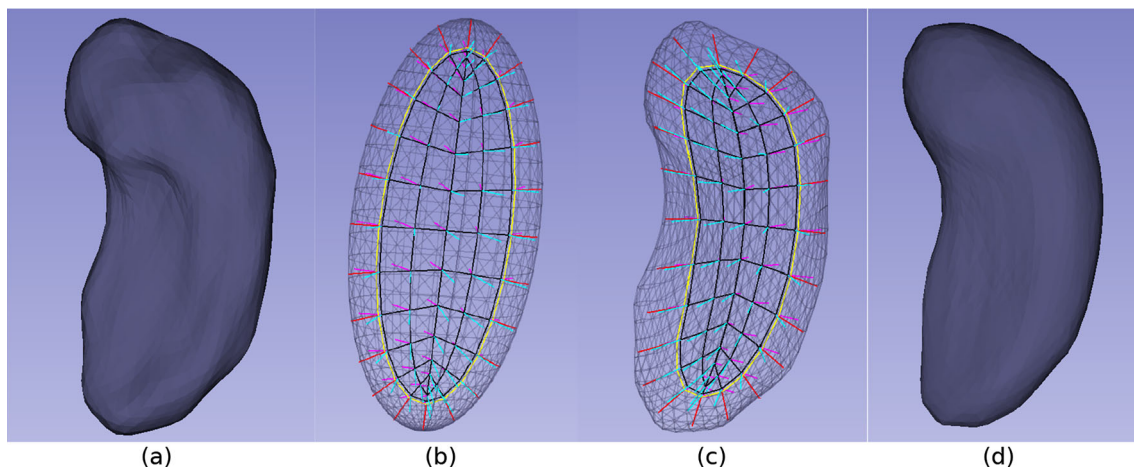
Fig. 2 Fit an s-rep to a hippocampus and derive its implied boundary from the s-rep. Panel **a**: SPHARM-PDM representation of the segmented boundary of a hippocampus. Panel **b**: A near ellipsoid (black transparent mesh) that is diffeomorphic to the hippocampal bound- ary. The ellipsoidal s-rep is discretized, yielding skeletal points (black grid points) and discrete spokes (colored line segments). Panel **c**: The discrete s-rep fit to the hippocampus. Panel **d**: The implied boundary derived from the hippocampus s-rep (Color figure online)

that projects shape descriptors onto a unit hypersphere and then Euclideanizes the spherical variables via PNS. Section 5 discusses the transformation ψ that extracts the joint shape variation from the PNS blocks.

3 S-rep Implied Boundary Points

This section discusses the shape model that we use to represent two-object complexes. Because segmented boundaries of anatomic structures are often noisy, skeletal representations (s-reps) are designed to provide robust and rich geometric features of objects. Importantly, geometric features provided by s-reps are designed to have good correspondence for joint analysis of multi-object complexes, leading to interpretable analysis results, as shown in later experiments.

An s-rep consists of a skeleton and "spoke" vectors defined on the skeleton. These spokes point from the skeleton to the boundary of an object. Compared to deformation-based shape models that are sensitive to ambient space deformations (see e.g., [16,19]), s-reps only capture interior and boundary geometric features of an object [39]. Different from other skeletal representations (e.g., [15,56]), s-reps are *fitted* to objects to have consistent skeletal topology across a population (see e.g., Fig. 2b, c). Such consistency allows us to have geometric features with good correspondence across a population.

Recently, Liu et al. [31] have proposed automatically fitting s-reps to *slabular* objects such as the hippocampus and the caudate. A slabular object refers to an object whose length is greater than its breadth, which is greater than its width. Such an object can be deformed to an ellipsoid via a dif-

feomorphism. Essentially, Liu's method deforms an s-rep of an ellipsoid to fit to an object. That ellipsoidal s-rep is consistently discretized so that spokes in the target object have correspondence across a population.

A fitted s-rep gives rise to a smooth mapping, so-called radial flow, from the skeleton to a set of level surfaces of radial flow [5]. These level surfaces have their own geometry (e.g., normals) without intersections within an object. Moreover, the radial distances $\tau \in [0, 1]$ are measured as fractions of spokes' lengths from the skeleton. The boundary of an object is equivalent to a level surface at $\tau = 1$, while the skeleton is a level surface at $\tau = 0$. We make use of landmarks on the level surface at $\tau = 1$ for each object. These landmarks are referred to as "s-rep implied boundary points", formed by the tips of spokes.

The s-rep implied boundary points provide good correspondence for each object across a population. The correspondence of these boundary points are determined by the correspondence of spokes. As shown in Fig. 2c, the primary spokes in each object have good correspondences across a population. Additionally, the interpolation method of an s-rep gives an arbitrary number of spokes [31]. This interpolation method uses the relative positions on the skeleton, which also provide correspondence across a population.

Figure 2 shows shape representations of an example hippocampus. In panel (a), the hippocampal shape is represented via SPHARM-PDM [45]. Though SPHARM-PDM gives a straightforward representation of segmented boundary geometry, it shows weaker robustness and inferior correspondence across a population than s-rep based shape representations (see e.g., [18,48]). Panel (b) shows an ellipsoid that is diffeomorphic to the hippocampal boundary in

panel (a). The ellipsoidal s-rep is consistently discretized, yielding the primary spokes shown as the line segments in red, cyan and magenta. Each skeletal point on the black grid is associated with two spokes (cyan and magenta) pointing to two sides of the ellipsoid. Each skeletal point along the edge curve (in yellow) is associated with a fold spoke (red) pointing to the crest curve of the boundary. This ellipsoidal s-rep is deformed to fit the hippocampus, as shown in panel (c). Then the s-rep is refined to have good geometric properties—for example, the spokes will not cross within the object so that the interior geometry of the object is smooth. Panel (d) shows the s-rep implied boundary, which is developed and used in this research. To obtain this implied boundary, we interpolate the refined s-rep so that we can obtain the same number of points with the SPHARM-PDM in panel (a).

4 Euclideanize Skeletally Implied Boundary Points

The above s-rep implied boundary points capture shape features coupled with pose and size variations. However, we want our joint shape analysis between the hippocampus and the caudate to be insensitive to translation and scaling of individual objects. To this end, we map the shape data onto a unit hypersphere by removing the position and size variation for each object. We detail this transformation in Sect. 4.1.

As a result of the above transformation, each object is transformed to a unit hypersphere that is also referred to as a pre-shape space. In order to make use of Euclidean methods of extracting joint shape variation, we Euclideanize the pre-shapes of each object, converting the pre-shapes to Euclidean shape features for each object. To do so, we adopt the method PNS, as discussed in Sect. 4.2.

4.1 Convert S-rep Implied Boundary Points to Pre-shapes

This research focuses on the joint shape variation between objects. The positions and sizes of objects should not affect the joint shape variation. To achieve joint analysis that is insensitive to positions and sizes of objects, we remove position and size variation by converting the coordinates of the s-rep implied boundary points to pre-shapes, as described below.

The position variation of an object can be removed by subtracting the coordinates of its centroid from the coordinates of landmarks [8]. Specifically, given a 3D object represented by m landmarks, let $X \in \mathbb{R}^{m \times 3}$ denote the shape feature matrix of the object. This object can be centered via a linear transformation $C \cdot X$, where the centering matrix $C = I_m - \frac{1}{m} 1_m 1_m^T$. In the centering matrix, $I_m \in \mathbb{R}^{m \times m}$ denotes an identity matrix and $1_m \in \mathbb{R}^{m \times 3}$ is a matrix of ones.

To remove the size variation, we denote $S(\cdot)$ as a function that measures the centroid-based size of an object. Specifically, let $\bar{X}$ denote the centroid of the object. The function $S(\cdot)$ is defined as

$$S(X) = \sqrt{\sum_{i=1}^{m} |X_i - \bar{X}|^2} \tag{5}$$

where X_i denotes the coordinates of the ith landmark. To take advantage of the centering matrix C, the function $S(X)$ can be written as

$$S(X) = |C \cdot X| \tag{6}$$

Combining the removal of position and size variation, we transform the shape matrix X via

$$Z_C = \frac{C \cdot X}{|C \cdot X|} \tag{7}$$

where $Z_C \in \mathbb{R}^{m \times 3}$ is referred to as a *pre-shape* because it is invariant to translation and scaling of the object represented by X. Accordingly, the pre-shape space is the space of all pre-shapes.

The pre-shape space is isomorphic to a unit hypersphere because any pre-shape is of unit size, i.e., $|Z_C| = 1$. Importantly, we center the data in the pre-shape space around the mean (i.e., the PNS mean) as detailed in Sect. 4.2. In some applications (e.g., [21]), shape features are also expected to be invariant to rotations of the object. There, a shape space is a stratified space of the pre-shape space, in which pre-shapes of different orientations are identified. Similar to previous research that was based on SPHARM-PDM (see e.g., [18,43]), our research preserves orientations of objects, restricting the data space to the pre-shape space.

As a result of the above transformation, we end with 2 unit hyperspheres. Figure 3 shows the resulting pre-shapes of a caudate nucleus (top row) and a hippocampus (bottom row). The left column shows the s-rep implied boundary points of each object, while the right column shows the pre-shapes transformed via Eq. (7). As shown in Fig. 3, the above transformation preserves shape characteristics despite the translation and scaling effects. Moreover, we find in our experiments that this transformation is helpful in classifying the ASD and non-ASD groups, suggesting that the positions and sizes of the objects are non-critical factors in distinguishing ASD among infants around the same age.

4.2 Euclideanize Pre-shapes

Our research benefits from the above transformation to pre-shapes not only because putting the data in the pre-shape

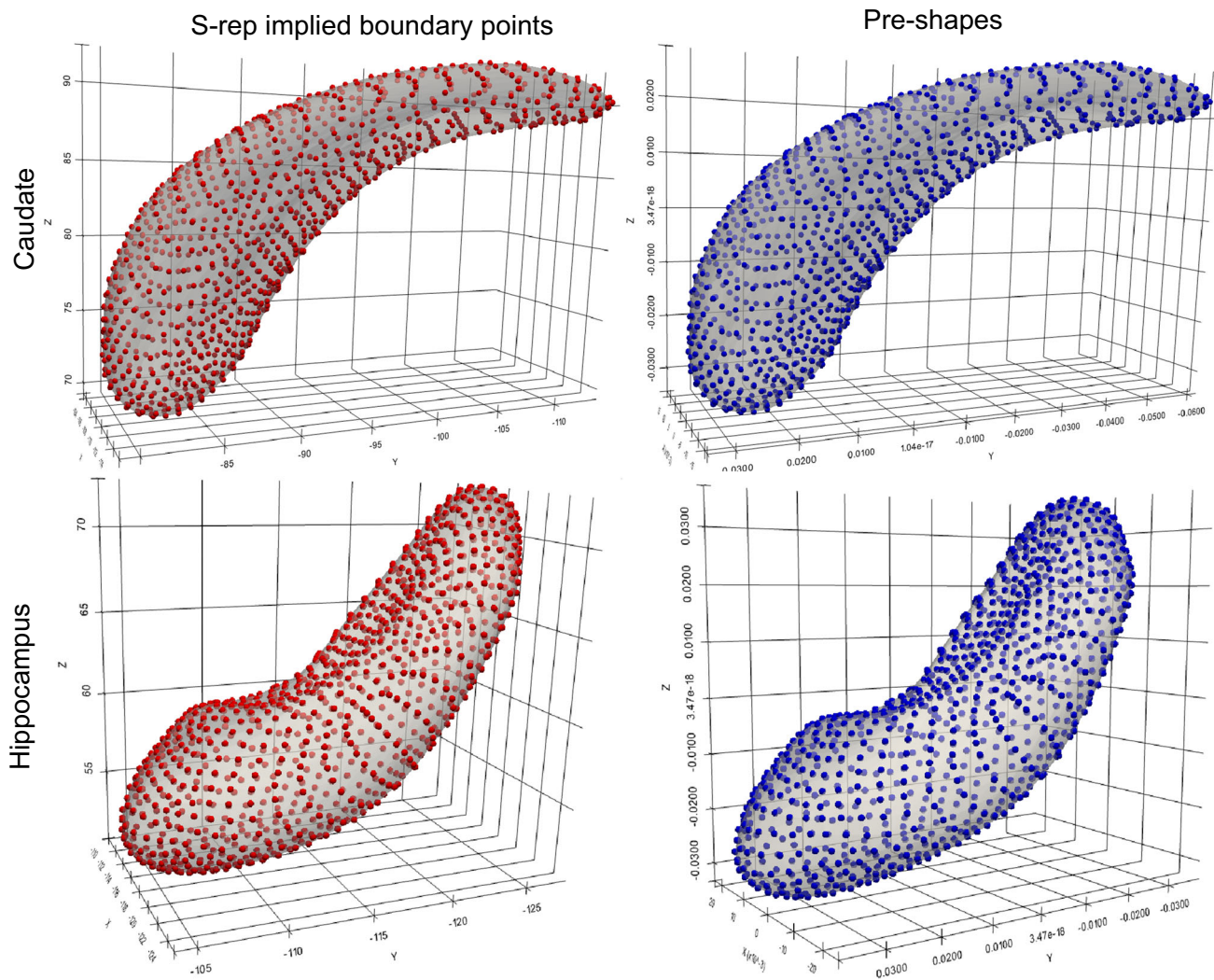**S-rep implied boundary points**

Pre-shapes

Caudate

Hippocampus

Fig. 3 Transform s-rep implied boundary points (red points) of a caudate nucleus (top row) and those of a hippocampus (bottom row) into pre-shapes that are represented by transformed points (blue points) via Eq. (7). Despite the translation and scaling effects, the geometry of the boundary is preserved. All these points are presented on smooth the implied boundary shown as transparent volumes underneath (Color figure online)

space removes the translation and scaling effects of each object, but also because the spherical geometry of the pre-shape space allows us to efficiently represent data.

In this paper, we choose PNS features [24] that give statistically efficient representations of pre-shapes in the following senses. First, PNS estimates a backwards mean that is more representative of spherical population than the Fréchet mean (see [37]). Second, PNS models the principal components in the pre-shape space via either a great circle (a geodesic curve) or a small circle (a non-geodesic curve), depending on the distribution of the data.

Specifically, PNS iteratively reduces the dimension of the unit hypersphere, yielding a hierarchy of subspheres (treated as generalized principal components) that fits the data by minimizing residuals (see Fig. 4). From these subspheres the

pre-shapes are represented by geodesic distances (restricted to the range of $[0, \pi]$). Eventually, these geodesic distances are taken as Euclidean representations of pre-shapes. We detail the process as follows.

Initial hypersphere. Let $X \in \mathbb{R}^{d \times n}$ be the n pre-shapes of dimension d, where $d \gg n$ in this paper. An initial hypersphere $\mathbb{S}^{n-1}$ can be obtained using Singular Value Decomposition (SVD) by removing components that have zero singular values.

Fit subspheres to data. Instead of only fitting great circles to single object data (see e.g., [13,21]), PNS fits a hierarchy of subspheres that are of decreasing dimensions from $\mathbb{S}^{n-1}$ down to $\mathbb{S}^0$, as shown in Fig. 4. At each dimension, the best fitting subsphere is obtained by minimizing the sum of squared residual geodesic distances along the surface of the
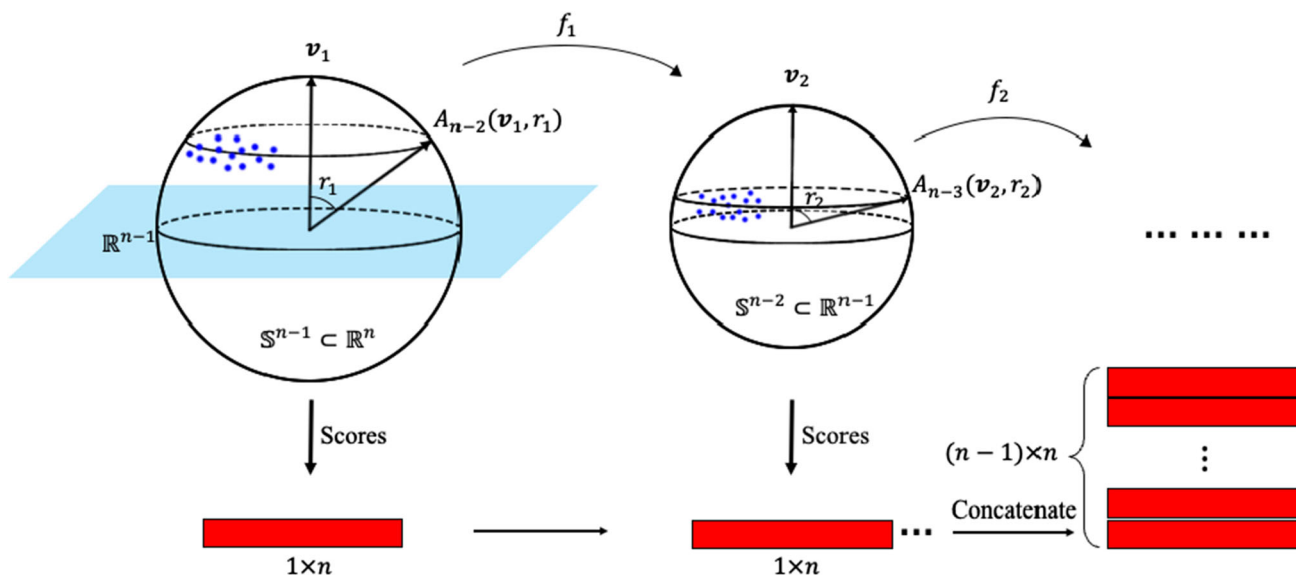
Fig. 4 Obtain PNS scores by fitting nested spheres to n samples, starting from the initial hypersphere $\mathbb{S}^{n-1}$. Blue dots illustrate pre-shapes on hyperspheres. Each subsphere A_{n-l-1} is parametrized by the center and radius (i.e., v_l and r_l), associated with a score vector of length n. The concatenation of the $n-1$ score vectors is taken as the Euclidean representations of the n samples

sphere. This best fitting subsphere is not necessarily a great circle because sometimes a small circle can better fit the variation which is natural to s-reps [6,37] and the s-rep implied boundary points. PNS computes the backwards mean on the nontrivial subsphere of the lowest dimension (i.e., $\mathbb{S}^1$). Then, this backwards mean is pulled back to every component in high dimensional spheres, yielding a representative mean on the nested spheres.

Compute scores from the fitted subspaces. In order to compute scores of each sample, which can be taken as Euclidean representations, PNS measures the geodesic distances from principal components that are represented by either a great or a small circle. In fact, each subsphere is the fitted principal component of its embedding sphere.

As a result, the nested subspheres of the initial hypersphere $\mathbb{S}^{n-1}$ produce $n-1$ score vectors, where n denotes the number of samples. Collectively, the two-object shape data are represented by two Euclidean blocks $\mathbb{R}^{(n-1)\times n} \times \mathbb{R}^{(n-1)\times n}$. In the following, we discuss extracting joint variation from these two Euclidean blocks, which forms the basis of our statistical analysis including hypothesis testing and classification.

5 Extract Joint Variation in Two-Object Complexes

From the above methods, each PNS block $\mathbb{R}^{(n-1)\times n}$ has n columns. Moreover, the two PNS blocks should align in columns in a way that the corresponding columns are from the same subject. The alignment of the two blocks in the score space allows us to extract their joint variation that is useful in discriminating the ASD and non-ASD group. We explain this alignment in Sect. 5.1.

Due to the alignment of columns, we refer to the row space $\mathbb{R}^n$ as "a score space". Thus, we treat the two-block data as two blocks of samples from a shared score space. In Sect. 5.2, we discuss extracting joint variation of two blocks of data using AJIVE within the PNS score space. Last, Sect. 5.3 discusses implications of joint variation from NEUJIVE.

5.1 Alignment in PNS Score Space

Though it is difficult to calibrate the two PNS feature spaces (two sets of nested subspheres), the two PNS blocks have a common score space. Moreover, as noted above, the joint shape variation of the hippocampus and the caudate should provide strong association with the development of ASD. It is natural to search the common PNS score space for the variation direction that points from the non-ASD cases to the ASD cases.

Two PNS score vectors (n-vectors) share a score space if the corresponding entries are about the same subjects. Specifically, we arrange columns in the two PNS blocks, aligning the ith column in the hippocampus PNS block and the ith column in the caudate PNS block both of which characterize the ith subject. By doing so, the correspondence of columns is determined by the column indices.

Within the shared score space $\mathbb{R}^n$ we search for the directions along which the hippocampus scores and the caudate

scores jointly vary. These directions together give a *joint variation space*, which is of prime interest in the following discussion. In Sect. 5.2 we discuss the method AJIVE that can simultaneously extract the joint and individual variation from the two PNS blocks.

5.2 Joint Analysis of Two-Block Euclidean Data

From an AJIVE viewpoint, each block of data is a combination of joint, individual and residual components. Specifically, let $X_k \in \mathbb{R}^{(n-1)\times n}$ denote the PNS block of the kth object, where $k = 1, 2$. Let J denote the joint component shared by the two objects. Let I_k and E_k, respectively, denote the individual and the residual component specific to the kth object. The feature matrix X_k can be decomposed as

$$X_k = J + I_k + E_k, \quad k = 1, 2 \tag{8}$$

Assuming that the joint and individual components are uncorrelated, AJIVE models the joint variation space orthogonal to every individual variation space. Because two PNS blocks share the same score space $\mathbb{R}^n$ as discussed above, we can define joint and individual variation spaces as subspaces of the score space $\mathbb{R}^n$. As such, the joint variation space and each individual variation space form a pair of complementary spaces in a certain subspace in $\mathbb{R}^n$.

We seek the mapping from the two-block data $\{X_k\}$ to the joint component J. To this end, AJIVE makes use of Principal Angle Analysis (PAA) to estimate the joint variation space. In our case, the intersection subspace of two PNS score spaces is taken as the joint variation space of the two PNS blocks, which is also a subspace in $\mathbb{R}^n$, as detailed below.

PAA of subspaces in a Euclidean space. PAA is used to analyze the relations between subspaces of a Euclidean space. It can achieve a robust estimation of the joint variation space when the subspaces in question are divergent in terms of dimension, unit or scale [2].

Principal angles (defined below) have been extensively investigated in measuring the difference between a pair of Euclidean subspaces (see e.g., [7,22,27]). Small or zero differences correspond to the joint variation space where statistical correlation arises. Consider in $\mathbb{R}^n$ two Euclidean subspaces of dimensions l and m, respectively, assuming that $l \leq m$. Let v_i and q_i denote vectors from the two subspaces, respectively, where $i = 1, \cdots, l$. The principal angles, i.e., the θ, of the two subspaces are defined as acute angles $0 \leq \theta_1 \leq \theta_2 \leq \cdots \leq \theta_l \leq \frac{\pi}{2}$ that are minima of

$$\theta_j = \min_{v_j, q_j} cos^{-1}\left(\frac{<v_j, q_j>}{||v_j|| \cdot ||q_j||}\right),$$

$$v_j \perp v_i, \quad q_j \perp q_i, \quad i \in [1, \ j-1] \tag{9}$$

where $< \cdot, \cdot >$ denotes the dot product. The pair of vectors v_j and q_j is called a pair of principal vectors, where $j = 1, \cdots, l$.

To evaluate the principal angles between the two Euclidean subspaces, PAA computes the principal angles as stated in the following lemma.

Lemma 5.1 *Let J and Q be two linear subspaces in $\mathbb{R}^n$, and let the rows of a matrix $M_J \in \mathbb{R}^{l\times n}$ and the rows of a matrix $M_Q \in \mathbb{R}^{m\times n}$ be orthonormal basis vectors for J and Q, respectively. The singular values σ_i of the matrix $M_Q M_J^T \in \mathbb{R}^{m\times l}$ relate to the solution of Eq. (9) via*

$$\sigma_i = cos\,\theta_i,$$
$$i = 1, \cdots, l \quad and \quad \sigma_1 \geq \sigma_2 \geq \cdots \geq \sigma_l \geq 0. \tag{10}$$

In practice, because of noise in real data, the principal angles can not equal 0 with probability 1. To address this problem, AJIVE estimates the basis vectors of the intersection space by selecting small enough principal angles. In the following, we detail how we use AJIVE to achieve a robust estimation of the joint variation space of two PNS blocks.

Orthonormalize PNS scores via low rank approximation. Because PAA requires orthonormal basis vectors of two Euclidean spaces in $\mathbb{R}^n$, the first step of AJIVE is to obtain orthonormal score vectors from the two PNS blocks. This orthonormalization can be achieved via SVD. Moreover, the operations of SVD on the two blocks can put negligible variation in the residual component E_k (see Eq. (8)) to avoid spurious correlation. The number of negligible components is determined by choosing an *initial rank r_k*.

Specifically, let $U_k S_k V_k^T$ be the result from SVD of the block $X_k \in \mathbb{R}^{(n-1)\times n}$, where U_k and V_k^T are orthonormal matrices. By choosing an appropriate initial rank r_k, we can simultaneously truncate (1) the columns of U_k, (2) the rows of V_k^T and (3) the rows and columns of S_k such that the negligible singular values are removed. As a result, we obtain the approximated left singular matrix $\hat{U}_k \in \mathbb{R}^{(n-1)\times r_k}$, the approximated singular value matrix $\hat{S}_k \in \mathbb{R}^{r_k \times r_k}$ and the approximated right singular matrix $\hat{V}_k^T \in \mathbb{R}^{r_k \times n}$. As a result, the low rank approximation of X_k can be written as $\hat{X}_k = \hat{U}_k \hat{S}_k \hat{V}_k^T$. Importantly, the rows in $\hat{V}_k^T$ give orthonormal basis vectors of $\hat{X}_k$'s score space, in which the joint and individual variation space are defined.

Estimate joint variation space. Next, we use AJIVE to select principal angles that are associated with basis vectors of the joint variation space. AJIVE calculates the principal angles based on SVD of the concatenation of the $\hat{V}_k^T$'s, according to Lemma 5.1. The pairs of principal vectors with large enough singular values (equivalently, small enough principal angles) are used to form the basis vectors of the joint variation space [12].

The joint component J is the projection of $\hat{X}_k$ into the joint variation space, capturing the variation driven by common factors of the two blocks. Therefore, we expect that in our data the joint shape variation of the hippocampus and the caudate from NEUJIVE is strongly associated with the development of ASD. Moreover, because this joint component integrates information from multiple blocks, the jointly varying features are expected to be insensitive to demographic differences [42]. Hence, the operation $\psi(\cdot)$ should enhance the discriminatory power of the two PNS blocks.

Individual variation. In addition to the joint variation space, individual variation that is specific to each PNS block is also of use in some applications. After extracting the joint components, AJIVE computes the individual components I_k using the orthogonality condition between J and I_k. By doing so, the resulting joint and individual components together provide a comprehensive understanding of the variation of each block. Though we focus on the joint component in this paper, we discuss potential applications of individual components in Sect. 8.

5.3 Implication of Ranks in NEUJIVE

The rank of the joint component J from NEUJIVE is the joint rank r (see Eq. (3)). This section distinguishes the joint rank r from the initial ranks r_k. First, we discuss the implication of the joint rank r computed by NEUJIVE. Then we discuss the choosable initial rank r_k for each PNS block.

The joint rank r from NEUJIVE indicates the classes/subclasses in the data. This rank is determined by the dimension of the joint variation space. Assume that the joint variation space from NEUJIVE consists of r basis vectors in $\mathbb{R}^n$, where $r \leq min(r_k) \leq n$. The number of the basis vectors has to do with (1) common characteristics of the two blocks (e.g., the severity of ASD) and (2) the degree to which the two blocks are correlated with the common characteristics. Therefore, the joint rank can be large in data of notable diversity (e.g., samples from many subtypes of the disease), while the joint rank can be small when the samples tend to be homogeneous. Particularly, $r = 0$ when there is a degenerate joint variation space due to the absence of significant correlation between blocks.

As noted above, the critical choosable parameter is the initial rank in approximating each block of data. This parameter directly determines the amount of signals passed to PAA. Also, the parameter determines the rank of the residual component. Specifically, in extracting joint shape variation of the hippocampus and the caudate, an over-rank setting leads to noisy input to PAA. The extraneous noise can prevent PAA from effectively extracting joint shape variation. Consequently, the joint shape variation may show weak association with the development of ASD. In contrast, an under-rank setting can dismiss the joint shape variation in the approxi-

mated matrix $\hat{X}_k$, which also prevents PAA from effectively extracting joint shape variation. In our experiments, we use cross-validation to choose an appropriate rank in the classification problem. Alternatively, Feng et al. [12] provide a means of choosing this parameter by inspecting the scree plot of each block. The optimal rank is chosen around the elbow position of the curve. This method can be useful in some applications, e.g., hypothesis testing. However, it is often difficult to manually choose the optimal rank in classification where a number of random experiments need to be done automatically.

6 Relevant Work

In this section we review related data integration methods. These are compared with our methods in Sect. 7. These other methods include Consensus PCA (CPCA) [54], JIVE [32], Generalized Canonical Correlation Analysis (GCCA) [44], Partial Least Squares (PLS) [53], Hierarchical PCA (HPCA) [52] and DISCO-SCA [49].

A straightforward approach to obtain the basis for the joint variation space is via a multi-block Principal Component Analysis (PCA) on the composite matrix $\{X_k\}$, which is called Consensus PCA (CPCA) [54]. However, the principal directions resulting from this approach can be dominated by the block of relatively larger variability, ignoring the joint variation.

Alternatively, Lock et al. [32] proposed Joint and Individual Variation Explained (JIVE) to decompose data into three structures, namely, the joint, individual, and residual structures. With this decomposition model, the method iteratively decomposes the data via minimizing the residual components. However, because JIVE estimates the dimension of the joint variation space via a permutation test, it is likely that JIVE can overestimate the joint component by inappropriately including individual components [12]. To address this problem, AJIVE proposes a more robust estimation of the joint variation space, leading to more robust joint components. Moreover, AJIVE is shown to be more computationally efficient than JIVE.

Another direction of multi-block data analysis is based on Canonical Correlation Analysis (CCA) [20] that maximizes the correlation over all possible directions, yielding pairs of canonical loadings $\{u_k \in U_k | k = 1, \cdots, K\}$, where U_k is the left singular matrix of X_k. However, the canonical loadings are not well-defined in HDLSS problems. Moreover, Shen et al. [44] point out that it is not necessarily beneficial to include additional datasets in classification with CCA. The researchers propose GCCA that can jointly analyze more than 2 datasets. Moreover, they show that GCCA can help the classification when some sufficient conditions are satisfied. This work shows an example of classification where an unsu-

pervised learning is followed by a supervised classification. Also, in the classification of real datasets, the researchers adopt an embedding method called Multi-Dimensional Scaling (MDS [46]). Importantly, the embedding via MDS and the dimension reduction via GCCA make no use of class labels. The classification splits training and test data from GCCA's results, which we call post-feature-selection in our classification experiment. However, the GCCA directions that maximize the correlation may not produce jointly varying patterns regarding two blocks. The inconsistent varying patterns in two blocks lead to inconsistent interpretation of various joint components. Moreover, this inconsistency complicates model selection.

Different from CCA, Partial Least Squares (PLS) [53] directions are the directions in feature spaces that maximize covariance instead of correlation. However, the resulting scores can be biased by structured noise, which is defined as systematic variation that is not linearly correlated between blocks (see [23] Section 4.2 for more details). To avoid the bias due to structured noise in standard PLS, Hierarchical PLS (HPLS) applies PCA on the data matrix prior to fitting a PLS model. As a result, the model can have better interpretability than standard PLS (see e.g., [28]). Alternatively, Trygg et al. [47] propose removing structured noise of two blocks via projections orthogonal to PLS components, yielding a method called O2-PLS. Due to the orthogonal projections, this method provides good interpretation of structured noise for each block. However, the joint variation space is different across blocks. The multiple joint variation spaces are not necessarily orthogonal to individual variation spaces, which might deteriorate the interpretability of the joint components.

Deun et al. [49] propose DISCO-SCA to simultaneously decompose the joint and individual components from multi-block data. This method first extracts the residual component via Simultaneous Component Analysis (SCA). Then it rotates the SCA components towards an optimal user-defined target matrix. Compared to AJIVE, DISCO-SCA rotates the concatenation of the joint and the individual components. This leads to orthogonal constraints between individual components across blocks. Such a restrictive constraint rarely corresponds to biological behaviors [26].

7 Experiments

This section aims to validate the effectiveness and robustness of the proposed method on both simulated and real data. In Sect. 7.1, we show that by extending AJIVE to NEUJIVE we can extract useful joint variation from two-block non-Euclidean data. Then in Sect. 7.2 we show the effectiveness of our method in extracting joint shape variation in simulated 2D objects. Different from Sect. 7.1, each block of the

simulated 2D objects has two groups, formed by a common process. Last, we assess our method in the context of a real dataset. To this end, in Section 7.3 we describe a shape data set (of subcortical structures) from the Infant Brain Imaging Study (IBIS) network. Sections 7.4 and 7.5 show hypothesis testing and classification of ASD and non-ASD on the subcortical structures' shape. Finally, we interpret the joint shape variation of the structures (the hippocampus and the caudate) related to ASD in Sect. 7.6.

7.1 Joint Components of Two-Block Non-Euclidean Data

In this section, we aim to verify the effectiveness of NEUJIVE for the joint analysis of two-block non-Euclidean data in a toy example. To this end, we simulate two correlated data blocks lying on $\mathbb{S}^2$, in which the joint component is created via a known function.

The two blocks of simulated data can be visualized as the colored points in the left column of Fig. 5. We simulate the data via the following steps:

1. We generate a joint component (a small circle) in the tangent space at the north pole of $\mathbb{S}^2$.
2. We generate an individual component for each block in the tangent space at the north pole of $\mathbb{S}^2$.
3. We map the generated data, which sum the joint component and the individual component, from the tangent space onto the sphere.
4. We rotate the above spherical data centered at the north pole to other places on the sphere.

Joint component. Because important modes of variation from s-rep based models tend to follow small circles (see [37] Section 6.1 for more details), we simulate a joint component along a small circle respective to each block. We sample 50 random variables θ from the uniform distribution $\theta \sim \text{Uniform}(0, \frac{3}{2}\pi)$. Then we map the θ's onto a unit circle, yielding circular points of coordinates $(\cos\theta, \sin\theta)$. We multiply the coordinates with block-specific constants a_k to have different radii of the circles across the two blocks, where $k = 1, 2$.

Individual component. In addition to the above joint component, we generate some random variables for each block. We sample independent two-dimensional Gaussian variables $\epsilon_1 \overset{i.i.d}{\sim} N(0, 1)$ and $\epsilon_2 \overset{i.i.d}{\sim} N(0, 1)$. The sum $a_k e^{i\theta} + \epsilon_k$ of the joint and individual components forms a noisy circular distribution on a tangent plane centered at the north pole of the sphere.

Map and rotate. The simulated data in the tangent space are then mapped onto $\mathbb{S}^2$ via the Exponential map $Exp(\cdot)$ centered at the north pole. Finally, we rotate the data from
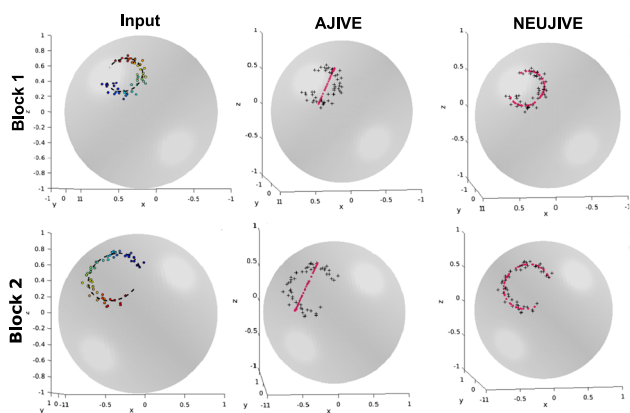
Fig. 5 Left column shows simulated two blocks of points on $\mathbb{S}^2$. The data tend to lie along a small circle with joint location on the circle indexed by the colors of points. The middle column shows the joint structure (magenta points) estimated by AJIVE in $\mathbb{R}^3$. This AJIVE joint variation follows a linear pattern. The right column shows the joint structure (magenta points) estimated by NEUJIVE. This NEUJIVE joint structure captures the actual joint variation pattern in the two blocks

the north pole to places that are specific to each block via rotations $g_k(\cdot)$, which result in

$$X_k(\theta) = g_k(Exp(a_k e^{i\theta} + \epsilon_k)) \qquad k = 1, 2 \qquad (11)$$

The left column in Fig. 5 shows the simulated two blocks X_1 and X_2 in the data space $\mathbb{S}^2$. The joint component of X_1 and X_2 follows small circles on $\mathbb{S}^2$, shown as the black dashed curves. The latent variables θ are indicated by colors as one moves along the small circles.

As shown in the right column of Fig. 5, NEUJIVE can effectively extract useful joint structures (magenta points) that follow a small circle pattern. In the middle column, the joint structures (magenta points) estimated by Euclidean AJIVE are far from the underlying joint variation pattern. In particular, the joint component from AJIVE follows a linear pattern instead of a circular pattern. Thus, the result from NEUJIVE provides a mode of variation that is much more descriptive of the actual joint variation in the data.

This toy example demonstrates that our method can effectively capture the joint variation between multi-block non-Euclidean data. We owe this effectiveness to the efficient representation of PNS scores. Moreover, the effectiveness of NEUJIVE remains when the joint component follows different patterns across blocks (see Appendix A). Due to space limitations, we show in Appendix A the Root Mean Square Error (RMSE) of the estimated joint structures via NEUJIVE under various levels of noise.

In addition to the joint component, NEUJIVE also results in reasonable individual components for respective block, clustered around the PNS mean. Because we focus on the joint variation in this paper, we show the individual component in Appendix A (see Fig. 11).

We have also tried GCCA, O2-PLS [3] and DISCO-SCA to decompose this toy dataset. However, we failed to find meaningful components on the sphere. We suspect that the failure is due to the difficulties of extracting joint variation in feature space after many nonlinear transformations on θ's in Eq. (11).

7.2 Joint Shape Analysis in Toy Classification

Beyond the above example, we also want to show that NEUJIVE can extract useful joint variation from two blocks each of which has two groups. To this end, we design the two groups to be formed by a common process in the two blocks. By doing so, the joint variation of the two blocks should be associated with the common process and thus be useful in classifying the two groups.

In particular, we simulate two blocks of shape data formed by 2D landmarks. The simulated data is analogous to the real shape data (see Section 7.3) of our interest in the following senses. First, the simulated shape are obviously different across the two blocks, analogous to the hippocampus and the caudate shape. Second, we impose on the two blocks a common process (via full Procrustes deformation[2]) to form two groups. This common process acts as the development of ASD, which simultaneously changes the shape of the hippocampus and the caudate. Last, it is difficult to classify the two groups within each block because the two groups have close means, which is also the case in classifying ASD vs. non-ASD using either the hippocampus or the caudate shape. In such scenarios, NEUJIVE can effectively extract joint shape variation that is associated with the group difference.

Figure 6 shows the simulated two data blocks, in which the two groups are denoted as the red and the blue. In this simulation, we start with a dataset from [9] in which eight 2D landmarks are sampled on each of the skulls of 29 male adult gorillas, shown as the blue circles in the top left panel. Then we create another group via a deformation φ [9], yielding the landmarks shown as the red crosses in the top left panel.

Next, we create a secondary block of data for the purpose of joint analysis, shown in the bottom left panel of Fig. 6. This secondary block is designed to have notably different shape from the above data block. In addition, the two groups in the secondary block are designed to be formed via the common process φ. Specifically, we first move the top-most landmarks in the top left panel to be farther away. Then we rotate all landmarks by 45 degrees. These modified landmarks are shown as the blue circles in the bottom left panel. Second, we apply

---

[2] While Procrustes alignment is normally used to preprocess shape data, our simulation instead uses this alignment to produce a geometric transformation that is sensitive to NEUJIVE and that forms the group difference.
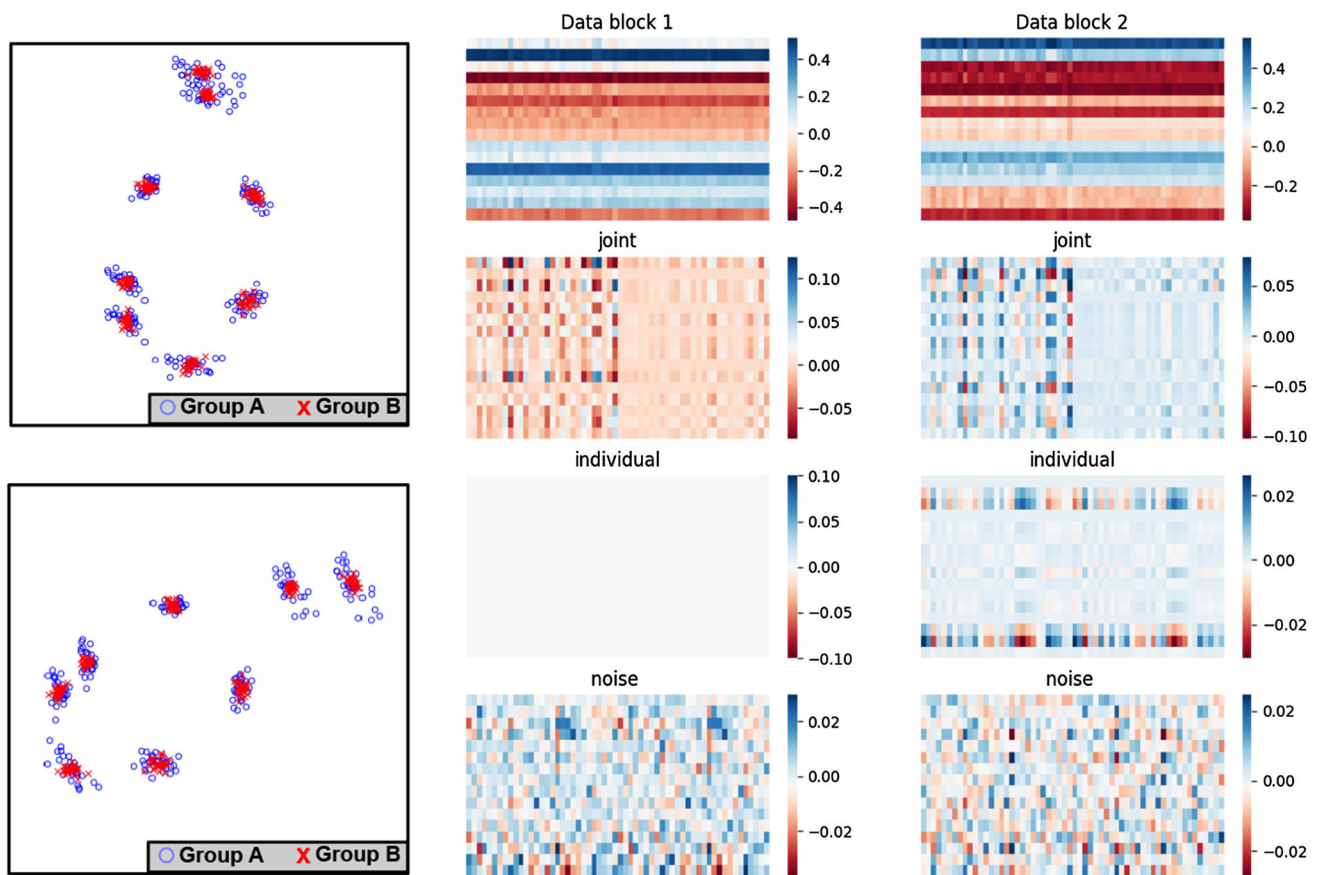
Fig. 6 Joint analysis of two blocks shape data formed by 2D landmarks from male gorillas' skulls. The left column shows the two blocks: block 1 (top) and block 2 (bottom). Each block has two groups (shown as the blue circles and the red crosses). We detail the generation of the two blocks in the text. The right two columns show the heat maps of the PNS matrices (the top row), the joint structures (the second row), the individual structures (the third row) and the residuals (the last row). The color represents the entry values of each matrix. See the text for detailed interpretation (Color figure online)

the deformation φ on the modified landmarks, forming the red group shown as the red crosses.

The above two blocks of landmarks with two groups form the input of NEUJIVE. Specifically, let $X_G \in \mathbb{R}^{16 \times 29}$ denote the original landmark matrix of the gorillas' skulls. The red group in the first block can be written as $\varphi(X_G)$. The concatenation of the two groups forms the first block X_1 of NEUJIVE. As we create the secondary block, we obtain the modified landmarks denoted as $\widetilde{X}_G \in \mathbb{R}^{16 \times 29}$. Likewise, the red group in the second block can be written as $\varphi(\widetilde{X}_G)$. The concatenation of $\widetilde{X}_G$ and $\varphi(\widetilde{X}_G)$ forms the second block X_2. In total, the inputs of NEUJIVE are organized as

$$
\begin{aligned}
X_1 &= [X_G \quad \varphi(X_G)] \in \mathbb{R}^{16 \times 58} \\
X_2 &= [\widetilde{X}_G \quad \varphi(\widetilde{X}_G)] \in \mathbb{R}^{16 \times 58}
\end{aligned}
\tag{12}
$$

We present the resulting components from NEUJIVE in the right two columns of Fig. 6. We obtain the pre-shapes of X_1 and X_2 by centering and normalizing each shape by the centroid size, yielding two pre-shape matrices. To each matrix, we apply PNS to obtain the PNS feature matrix shown in the top row. The colors in the heat maps represent the entry values of the PNS features of X_1 (the middle column) and X_2 (the right column). The other rows show the entry values of the matrices resulting from the joint analysis of the two PNS blocks. The resulting NEUJIVE components include (1) the joint components (shown in the second row), (2) the individual components (shown in the third row) and (3) the residual components (shown in the last row).

In Fig. 6 we can observe notable patterns from the joint components, as compared to the input matrices, the individual components and the residual components. Across all these matrices, columns are samples, while rows are features. We can find clearly different patterns between the two groups of samples in the joint component of every block. This visualization suggests that the joint component from NEUJIVE focuses on the common factors that form the two groups. As

Table 1 Test performance using different features in classification

Features	X_1	X_2
Landmarks	0.44 ± 0.15	0.46 ± 0.15
PNS	0.46 ± 0.12	0.48 ± 0.13
Euclidean AJIVE	0.53 ± 0.14	0.52 ± 0.12
Spherical AJIVE	0.68 ± 0.08	0.66 ± 0.08
NEUJIVE	$\mathbf{0.75} \pm 0.09$	$\mathbf{0.72} \pm 0.1$

Bold values indicate best performance among the compared methods

such, we make use of the joint component in classifying the two groups.

The individual components also are as expected in both blocks. Because of the facts (1) that the first block uses the initial rank of 2, while the second block uses the initial rank of 3 and (2) that the joint variation is rank 2, there is no individual variation specific to the first block.

To demonstrate that the joint shape variation improves the classification between the red and the blue group, we compare in the following (1) the classification using the joint component from NEUJIVE, (2) the classification using the landmarks and (3) the classification using the joint component from other joint analysis methods including AJIVE.

To classify the two groups, we train a robust linear classification method called Distance Weighted Discrimination (DWD). This has been shown to have better properties than the support vector machine by [33]. We randomly select 80% of the data in the training while we use the remaining in the test. To avoid the bias due to splitting the data, we repeat this experiment 100 times. Table 1 reports the average test accuracy ($\pm$ standard deviation) over all the repetitions. The classification of each block uses various sets of features (corresponding to the rows of Table 1): (1) the original coordinates of landmarks (the first row), (2) the PNS scores (the second row), (3) the joint structures from AJIVE on the original coordinates (the third row), (4) the joint structures from AJIVE on the spherical coordinates (the fourth row) and (5) the joint structures from NEUJIVE (the fifth row).

From Table 1 we find that the joint component from NEU-JIVE (the last row) improves the classification performance compared to raw landmarks (the first row) by a large margin. It is difficult for a linear classifier to learn a good decision boundary from the coordinates of landmarks. Moreover, we find that the Euclidean AJIVE can capture some group difference. Yet, due to the complexity of the data space, the group difference is relatively weak in AJIVE's joint component, compared to those from Spherical AJIVE and NEUJIVE. Importantly, NEUJIVE's joint component more strongly indicates the group difference than those of Spherical AJIVE. We owe this advantage to the statistically efficient data representation by PNS.

7.3 Autism Data for Multi-Object Shape Analysis

From this section on, we analyze the shape of subcortical structures from 174 infants. These structures are segmented [50] from MRI images of the subjects around 6-months-old. There are 33 of the infants who were diagnosed as autistic later and 141 of these were shown not to have developed autism.

We focus on complexes that consist of the left hippocampus and the left caudate. Each object is represented by a triangular mesh using SPHARM-PDM [45]. We fit s-reps to each object and extract 1002 implied boundary landmarks from the s-reps, as described in Sect. 3.

In the following, we first check if there exists statistically significant difference between ASD and non-ASD in the joint component from NEUJIVE. We check the statistical significance via a hypothesis test, as discussed in Sect. 7.4. Then we conduct classification experiments in Sect. 7.5. Section 7.6 shows an interpretation of the joint component of the hippocampus and the caudate.

7.4 Hypothesis Testing

Our hypothesis test aims to verify whether the difference between the two groups (ASD vs. non-ASD) is statistically significant in the joint variation space. Because the sample size is small, the hypothesis test should be based on permutation testing ideas. To this end, we accomplish this task in the following steps.

We start from s-rep implied boundary points of the hippocampus-caudate pairs, each of which is associated with a class label (i.e., ASD or non-ASD). We separately convert the landmarks of the hippocampus and those of the caudate into pre-shapes as described in Sect. 4.2. Then we apply NEUJIVE to the pre-shapes of the hippocampus and the caudate.

Figure 7 shows for various features the Explained Variance Ratio as a function of the number of eigenmodes. We choose s-rep implied points to remove non-systematic geometric details on the boundary. As a result, the s-rep implied boundary points give smooth geometric features across a population. Also, Fig. 7 suggests that PNS features (green curves) are more statistically efficient representations, especially for the caudate and for the hippocampus-caudate pair, as compared to the pre-shapes (orange curves).

Figure 7 also gives us a means of choosing initial ranks for low rank approximation. Considering the Explained Variance Ratio of PNS features from s-rep implied boundary points (s-rep PNS), we choose the initial rank 50. In this setting, NEUJIVE finds a joint component of rank 2 (i.e., $r = 2$ from Fig. 1c), which suggests very few common characteristics in our data, as discussed in Sect. 5.3. It turns out that these two
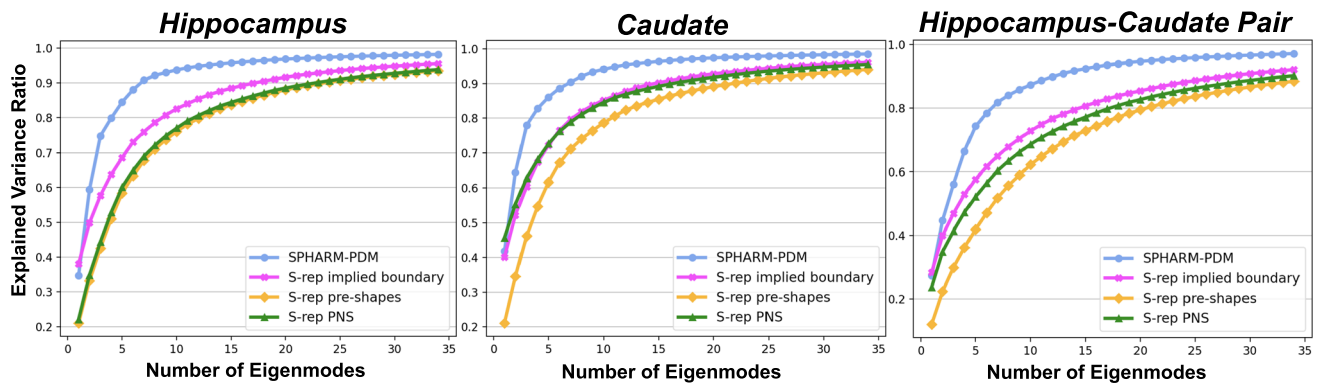
Fig. 7 The cumulated Explained Variance Ratio (EVR) of the first 35 eigenmodes vs. the number of eigenmodes. The left and the middle panel show the EVR of shape features from single objects—the hippocampus and the caudate, respectively. The right panel shows the EVR of concatenated shape features of the hippocampus-caudate pairs. Best viewed in color images (Color figure online)
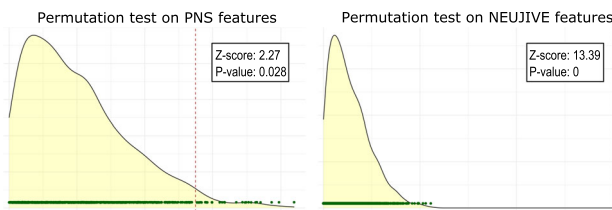

Fig. 8 The results from the permutation test of concatenated PNS blocks (left) and the test of NEUJIVE joint component (right). The green dots on the bottom of each figure represent the test statistics (i.e., MDs) from the permutations. The black curve represents the estimated density function of those MDs

dimensions give statistically significant difference between the ASD and non-ASD groups.

Within the two-dimensional joint variation space (a subspace in $\mathbb{R}^n$), we test the data projected on the unit vector between the means of the two groups with a permutation test, which is implemented by a method called Direction-Projection-Permutation (DiProPerm) [51]. We let DiProPerm generate 1000 random permutations and then compute the univariate statistic, i.e., Mean Difference (MD) between the two groups for each permutation.

Figure 8 shows the test statistics on the MDs in those permutations using two sets of features. The observed MDs of the two groups are at the positions of the vertical dashed lines. Along with the permutation statistics, we show the empirical p-values, which are the proportion of the permutations that have larger MDs than the observed MD. We also show the z-scores, which measure how many deviations that the observed MDs are above the average MD of their permutations. The p-values and z-scores together indicate statistical significance of group difference with respect to the test features. Smaller p-values and larger z-scores indicate more statistical significance of the group difference.

NEUJIVE joint components give statistically significant difference between the ASD and non-ASD groups, as shown

in Fig. 8 right. We found no permutations that have larger MDs than the observed MD, i.e., the empirical p-value equals 0. Moreover, the z-score (≈ 13.39) is relatively large, indicating strong statistical significance. As a comparison, we use the concatenated PNS blocks of the hippocampus and the caudate in the test, yielding less statistically significant difference, as shown in the left panel. Specifically, there is a small proportion ($\sim 2.8\%$) of permutations that have larger MDs between the ASD and non-ASD group than the observed MD.

Table 2 presents more comprehensive results from the hypothesis test using various sets of shape features. The first row shows the results from using the concatenation of s-rep implied boundary points. The second row shows the results from using the concatenation of Euclideanized PDMs with PNS. Comparing these two rows, we notice that the Euclideanization improves the discriminatory power of the shape features. Moreover, using joint structures from AJIVE (the third row) results in a more statistically significant difference between the two groups. The fourth row shows the results of our hypothesis test with NEUJIVE features. It demonstrates the advantages of using the joint shape variation in the test. The last three rows of Table 2 show the results from the compared joint analysis methods that are reviewed in Sect. 6. These methods can extract the correlation of features in high dimensional feature space. Yet, the group difference from these methods are not as significant as those from NEUJIVE.

7.5 Classification

Because joint shape variation captures correlated shape features from multiple objects, and because this correlation is closely associated with class labels, the joint components from NEUJIVE lead to statistically significant differences in the above hypothesis test. In this section, we attempt to

Table 2 Hypothesis testing of ASD vs. non-ASD with different joint features

	p-values $\downarrow$ [a]	z-scores $\uparrow$ [a]
Concatenate Implied PDMs	0.3106	0.3679
Concatenate Euclideanized PDMs	0.028	2.274
AJIVE [12]	0.0136	2.7714
NEUJIVE (ours)	**0**	**13.392**
HPLS [55]	0.1135	1.206
PNS + HPLS	0	4.4263
E-GCCA [44]	0.0169	2.0031

Bold values indicate best performance among the compared methods
[a] Smaller p-values and larger z-scores indicate more significant differences

exploit the joint components from NEUJIVE in classifying the ASD versus non-ASD group.

Because the joint analysis via NEUJIVE is based on the alignment of PNS score space, as discussed in Sect. 5.1, it is necessary to estimate the joint shape variation by pooling the training and test data. Oftentimes, the number of training and test samples are different. Therefore, the estimated joint shape variation space in the training domain is not readily transferable to the test domain. To address this problem, we pool the training data with the test data for the joint analysis via NEUJIVE. The resulting joint shape variation is the basis of training and testing a classifier. Because the process of producing joint shape variation does not make use of class labels, it is natural to compare with other similar classification methods such as the method using GCCA [44].

We obtain the joint shape features following steps similar to Sect. 7.4. We again use DWD as the classifier in this section. We compute the Area Under the ROC (Receiver Operating Characteristics) Curve (ROC-AUC) as the evaluation metric. Fig. 9a shows the ROC-AUCs as a function of initial ranks. From Fig. 9a we can see that the optimal performance results from the initial rank of about 50. Fig. 9a also shows that both the under-ranks ($r_k < 47$) and over-ranks ($r_k > 54$) can lead to poor performance in classification.

To select a good initial rank for the test data, we use five-fold cross-validation to select the optimal initial rank from 20 sets of NEUJIVE joint features. Specifically, we apply NEUJIVE to the pooled data with 20 different initial ranks. By observing the Explained Variance Ratio via s-rep PNS features in Fig. 7, we set the same initial rank for the hippocampus and the caudate PNS block. The 20 parameters result in 20 sets of NEUJIVE joint features. We apply the same partition of samples[3] to every set of NEUJIVE joint features into the training, validation and test data. To avoid bias due to splitting data, we generate 1000 random partitions of samples.

---

[3] We create a random partition of the samples into 10 roughly equal-sized subsets of the ASD group and likewise with the non-ASD group. We set aside one of the subsets from each group for testing and use the remaining subsets for training and validation.

We compared test AUCs from NEUJIVE with those from other multi-block analysis methods, including Hierarchical PCA (HPCA) [52], Consensus PCA (CPCA) [54] and Generalized CCA (GCCA) [44]. We show the histogram of the test ROC-AUCs in Fig. 9b. Our method (shown as the green curve) performs better than the compared methods.

Figure 9c shows the average test ROC-AUCs (from 1000 partitions) from NEUJIVE (the green bars) and the compared methods. In the classification using the joint structures of either the hippocampus or the caudate, our method significantly improves the average test ROC-AUC. This improvement benefits from both the Euclideanization via PNS and the focus on joint structures provided by AJIVE. Also, we find that the joint structures from NEUJIVE are almost consistent across blocks, shown as the green bars. As a comparison, the other methods yield notably different joint structures for the hippocampus block vs. for the caudate block.

7.6 Shape Differences in the Joint Variation Subspace

In medical applications, it is important to interpret the results from anatomic shape analysis. The results from NEUJIVE can be pulled back to the pre-shape space for understanding the joint shape variation patterns. In this section we demonstrate the interpretation of the joint shape variation of the hippocampus and the caudate from NEUJIVE.

Specifically, we show how to interpret the difference between the ASD and the non-ASD group in NEUJIVE's joint variation space. Given the NEUJIVE joint structure $J \in \mathbb{R}^{r \times n}$, we first separately average the columns of the ASD group and those of the non-ASD group, yielding a matrix $Y \in \mathbb{R}^{r \times 2}$. Then we map the matrix Y to the PNS hippocampus block and to the PNS caudate block, respectively, resulting in the hippocampus PNS features of two groups and the caudate PNS features of two groups. The two PNS blocks are both of dimension $(n-1) \times 2$. We apply the inverse PNS to obtain pre-shapes of the hippocampus
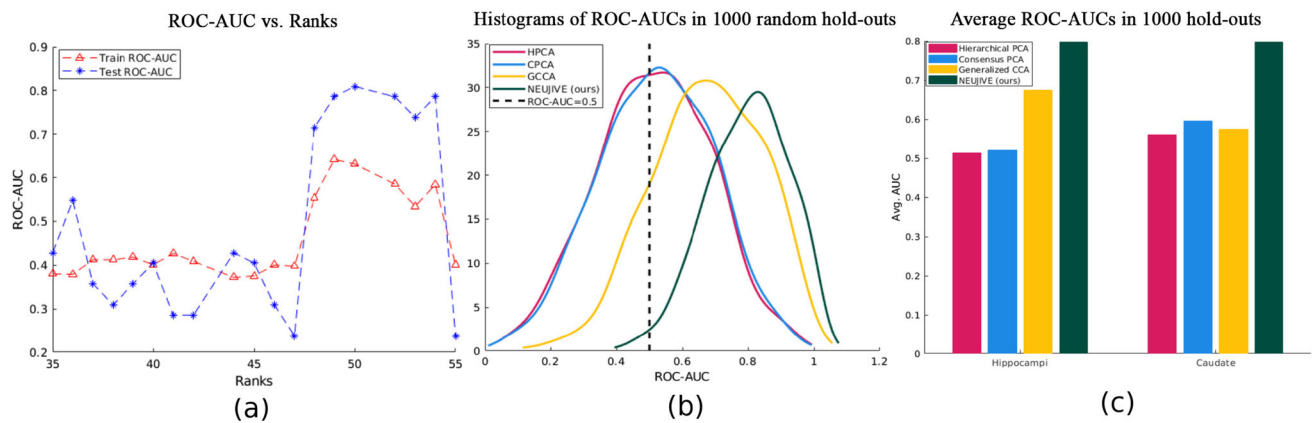
Fig. 9 Results from the classification using joint structures. **a** The AUCs in classifying ASD vs. non-ASD with NEUJIVE joint features vs. the chosen initial ranks. **b** The histograms of test AUCs using joint struc-tures of the hippocampus from different methods. **c** The average test AUCs from various methods using the joint structures of hippocampi (left part) and caudate nuclei (right part)
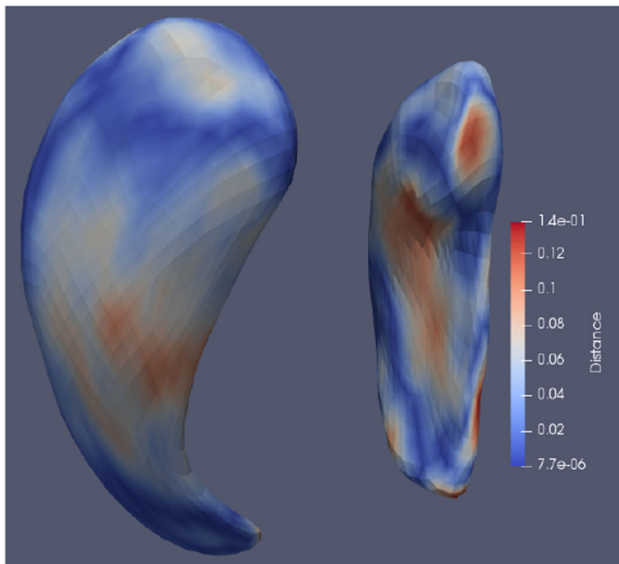

Fig. 10 The visualization of the group mean differences (in millimeters) captured in NEUJIVE joint variation space. The two groups are the autism and the non-autism group. These two groups have more difference in the red regions than in the blue regions (Color figure online)

and those of the caudate. Finally, we compute Euclidean distance for each object between the pre-shapes of the two groups.

The distances between the corresponding landmarks are shown in Fig. 10 as heat maps overlaid on a non-ASD hippocampus-caudate pair. Such heat maps suggest that some regions (the red) in the hippocampus and the caudate are more jointly associated with ASD than other regions (the blue). This visualization provides a means of understanding joint shape variation of multi-object complexes in the development of ASD.

8 Broader Impact

Though this research focuses on multi-object shape analysis, there are many possibilities to generalize our proposed methods to other applications. This section discusses a more general form of our methods. The general form leads to broader impact beyond multi-object shape analysis. Specifically, we discuss possible generalization (1) of data representations (2) of manifolds that the representations live on and (3) of Euclideanization methods. Next, we discuss potential applications of the individual variation component from NEUJIVE.

First, it is possible to have different representations of data in some applications. We only use s-rep implied boundary points in our research because these landmarks have good correspondence and also because it is rather simple to map the data to a unit hypersphere. However, other shape features from s-reps (e.g., spokes' directions) also provide useful information of an object. Such shape features often require a different mapping to manifolds and to the Euclidean representations (e.g., via Composite PNS [38]). Moreover, although this paper focuses on applications in two-object complexes, the methods are generalizable to multi-object complexes each of which contains more than 2 objects. Because PAA can accept multiple input Euclidean subspaces in $\mathbb{R}^n$ and output their joint variation space (also in $\mathbb{R}^n$), there are no theoretical barriers preventing the analysis of more than 2 objects. However, care is needed in the selection of objects. All the selected objects should be (strongly) associated with at least a common factor (e.g., disease of few subtypes). Otherwise, it is difficult to find the joint variation with PAA.

Second, our joint analysis method is applicable for the data not only on the cross-product of unit hyperspheres, but

also on the cross-product of general Riemannian manifolds (e.g., polysphere [11]) or stratified sets. The geometry of the manifolds determines the Euclideanization method, as discussed below.

Third, there exist various Euclideanization methods that map data on a manifold (or a stratified set) to a Euclidean space. The choice of the method should depend on the data properties. Principal Geodesic Analysis (PGA) [13], for instance, is used in capturing principal components of data in a Riemannian manifold. The Euclidean representation from PGA is expressed in terms of an orthonormal basis in the tangent space centered at the Fréchet mean. Regardless of the different choices of the basis, AJIVE can achieve consistent results from multiple PGA blocks because of invariance properties of PGA score spaces under rotations of the basis (i.e., orthogonal transformations multiplied on the left of $\phi(X_1)$ or $\phi(X_2)$ in Eq. (4)).

Last, although we focus on the joint shape variation in this paper, the individual shape variation can also be useful in some applications. In contrastive analysis (see e.g., [1]), multiple datasets are used to extract the distinctive variation. In this regard, the individual shape variation from NEUJIVE is useful to extract robust and meaningful patterns of interest. We leave this as our future research.

9 Conclusions and Discussion

This research aims to provide geometric and statistical methods for analyzing multi-object complexes. Despite the recent advances in the shape statistics field and in the multi-block data analysis field, there previously existed no methods that effectively extract joint and individual shape variation. This paper bridges the two fields, yielding a new method that can effectively extract joint shape variation from multi-object complexes.

We focus on the joint shape variation in two-object complexes in this paper. Because ASD simultaneously changes the shape of multiple brain structures including the hippocampus and the caudate, it is natural to assume that the shape of these related structures are jointly varying in the development of ASD. Under this assumption, an effective joint shape variation should be associated with the development of ASD. Therefore, we verify the effectiveness of NEUJIVE in the hypothesis test and classification between the ASD and non-ASD group. The interpretation of the joint shape variation may lead to interesting findings regarding the development of ASD.

Not only in the experiments with real shape data, we also verify our method in toy examples, showing notable advantages over our baseline method AJIVE. In analyzing the example with multi-block homogeneous data, NEUJIVE can effectively recognize the joint variation component (see

Sect. 7.1), regardless of the complexity of the feature spaces. In the toy example with multi-block heterogeneous data (of two groups), NEUJIVE focuses on the group difference in the joint structures and thus results in higher classification accuracy. These toy examples explain the advantages of NEUJIVE on multi-block non-Euclidean data analysis.

These experimental advantages result from our choice of the methods in this paper. First, to capture shape features of the hippocampus and of the caudate, we develop s-rep implied boundary points, which yield smooth geometric features with good correspondences across a population. Second, to obtain shape features that are insensitive to the pose and size variation, we convert s-rep implied boundary points into respective pre-shape space. Third, we adopt PNS to convert pre-shapes into Euclidean variables. The resulting PNS scores are insensitive to orthogonal transformations of features, making the Euclidean representations robust against rotations of objects. Moreover, the score spaces $\mathbb{R}^n$ of two PNS blocks share basis vectors with aligned columns, assuming columns are observations. This alignment allows us to extract joint shape variation of the two objects. Fourth, we use AJIVE to estimate the joint variation of the two PNS feature matrices, yielding low-dimensional jointly varying features.

In our future work, in addition to the potential applications discussed in Sect. 8, we also want to extend this research by explicitly accounting for the relations between objects [30]. Among selected objects that are likely associated with a disease, it is possible that within-object shape features of an anchor object correlate with its relations with other objects during the development of the disease. In such a scenario, the joint shape variation of within- and between-object shape features can provide interesting information about multi-object complexes.

10 Online Resources

We have provided python code that generates an arbitrary number of s-rep implied boundary points, given a triangular mesh from SPHARM-PDM. We also provide MATLAB and R code that can simulate the toy examples. Due to limited permission of sharing the ASD data, we only provide the code to reproduce the synthetic experiments in the repository (see https://github.com/ZhiyLiu/shanapy).

A Non-Euclidean Joint and Individual Variation Explained

In this section, we show more comprehensive experimental analysis of NEUJIVE.

First, it is of interest to show all NEUJIVE components of the toy example discussed in Sect. 7.2, which has homogeneous circular data in each block. In Fig. 11 the first row shows both the joint and the individual structures from NEUJIVE. The individual structures are designed as random variables from multivariate Gaussian (see Eq. (11)). Moreover, the top left cell in Fig. 11 shows that the individual structures (shown as blue dots) from NEUJIVE are distributed around the PNS mean as expected. As a comparison, AJIVE fails to find significant individual components in either block, as shown in the top right cell. Instead, the blue dots are the residual components resulting from AJIVE.

Second, we show the NEUJIVE components when the two blocks are of notably different variability in the bottom row of Fig. 11. Different from Sect. 7.2, the first block is generated via

$$X_1 = g_1(Exp(p(\theta) + \epsilon_1)) \qquad (13)$$

where $p(\theta)$ is a straight line in the tangent space at the north pole. A point on this line has coordinates $(\theta, 0.3\theta)$. The second block is still generated via Eq. (11). Moreover, to have Different Noise Levels (DNL) across the two blocks, we set different standard deviations of ϵ_k across the two blocks. The results show that NEUJIVE can still give effective estimation of the joint components regardless of the different variability between the two blocks.

Third, we investigate the robustness of the joint structures estimated by NEUJIVE as we increase noise. We simulate two blocks of data via Eq. (11), increasing the standard deviation of ϵ_k from 0.01 to 0.1. The simulated data under 3 different noise levels can be seen in Fig. 12 left, i.e., $\sigma(\epsilon_k) = \{0.01, 0.05, 0.1\}$. For each noise level, we compute the joint structure from NEUJIVE. We measure the Root of Mean Square Error (RMSE) between the NEUJIVE joint structures and the actual joint structures. The curves of RMSE versus noise levels of the two blocks are shown in Fig. 12 right. This figure shows that the RMSE is almost linearly increasing along with the increasing noise level.
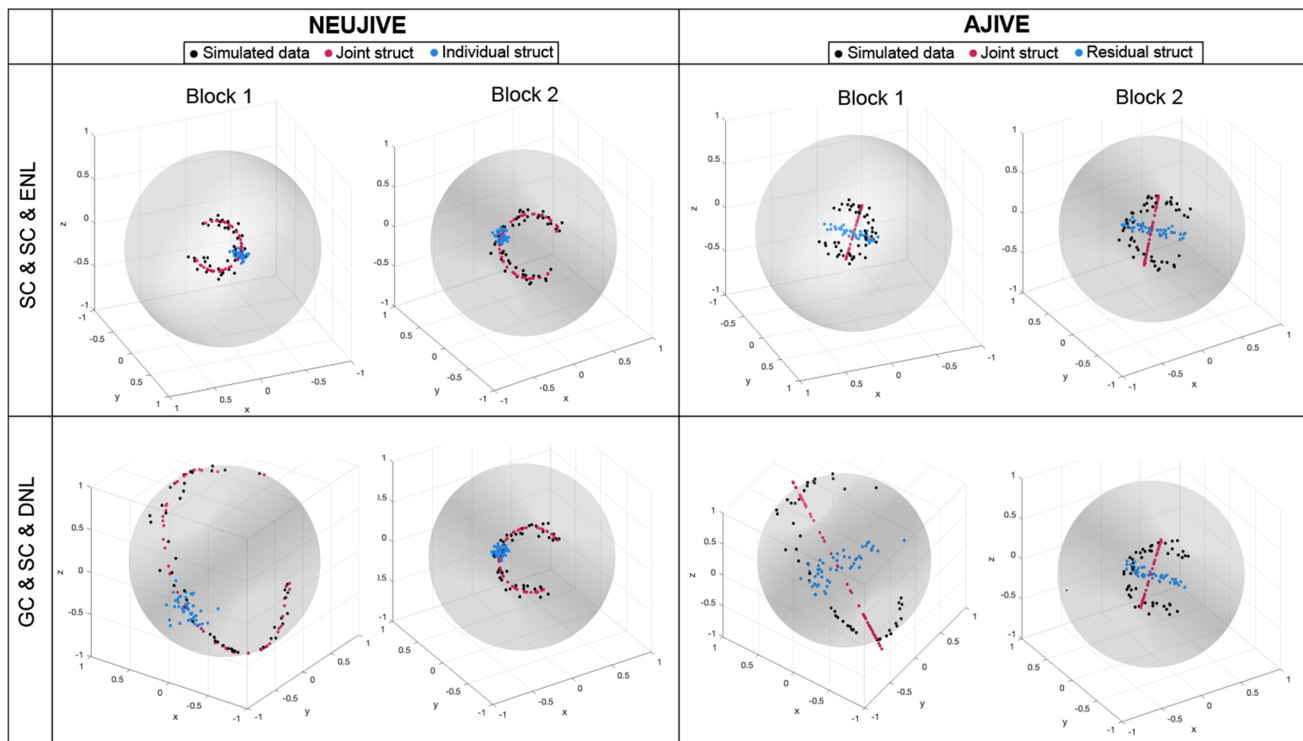

Fig. 11 Joint and individual structures from NEUJIVE on two correlated non-Euclidean blocks. The first row shows the simulation where the joint structures are designed as circular variables along Small Circles (SC) in the two blocks (see Eq. (11)). Moreover, the two blocks share the Equal Noise Level (ENL) in which ϵ_k share the same standard deviation. The second row shows a different simulation study. In this simulation, the joint component is designed to be a Great Circle (GC) in block 1. But this component follows a small circle in block 2. Moreover, the two blocks have Different Noise Level (DNL). On each sphere, the black dots are simulated data. The magenta dots are joint structures from each algorithm. The blue dots are individual structures from NEUJIVE and residual structures from AJIVE, respectively
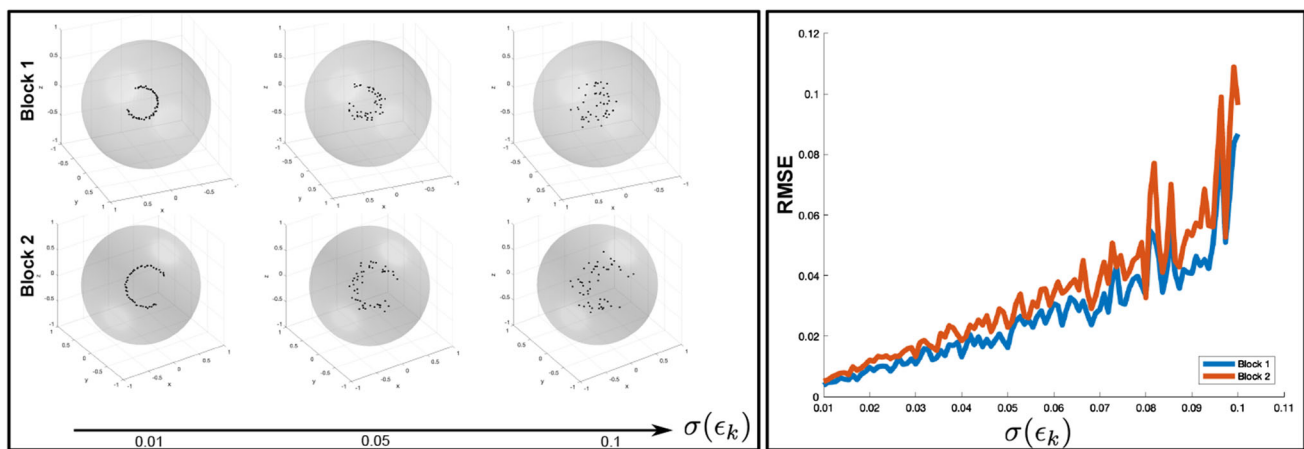
Fig. 12 Root Mean Square Error (RMSE) between the actual joint structures and NEUJIVE estimated joint structures as increasing the noise level. Left panel: Simulated data as increasing the standard deviation $\sigma(\epsilon_k)$ of noise from 0.01 to 0.05 and to 0.1. The two circular blocks are of different radii, i.e., $a_1 = 0.25$ while $a_2 = 0.35$. Right Panel: RMSE of the NEUJIVE joint structures of the two blocks as increasing standard deviation of noise. The red and the blue curve are, respectively, the RMSE of the block 1 and the block 2

References

1. Abid, A., Zhang, M.J., Bagaria, V.K., Zou, J.: Exploring patterns enriched in a dataset with contrastive principal component analysis. Nat. Commun. **9**(1), 1–7 (2018)
2. Björck, A., Golub, G.H.: Numerical methods for computing angles between linear subspaces. Math. Comput. **27**(123), 579–594 (1973)
3. Bouhaddani, S.E., Uh, H.W., Jongbloed, G., Hayward, C., Klaric, L., Kielbasa, S.M., Houwing-Duistermaat, J.: Integrating omics datasets with the omicspls package. BMC Bioinf. **19**(1), 1–9 (2018). https://doi.org/10.1186/s12859-018-2371-3
4. Cerrolaza, J., López Picazo, M., Humbert, L., Sato, Y., Rueckert, D., González Ballester, M.A., Linguraru, M.G.: Computational anatomy for multi-organ analysis in medical imaging: a review. Med. Image Anal. **56**, 44–67 (2019)
5. Damon, J.: Smoothness and geometry of boundaries associated to skeletal structures I: sufficient conditions for smoothness. Ann. línst. Fourier **53**, 1941–1985 (2003)
6. Damon, J., Marron, J.: Backwards principal component analysis and principal nested relations. J. Math. Imag. Vis. **50**(1), 107–114 (2014)
7. Deutsch, F.: The angle between subspaces of a Hilbert space. In: Approximation theory, wavelets and applications, pp. 107–130. Springer (1995)
8. Dryden, I.L., Mardia, K.V.: Statistical shape analysis. Wiley, Chichester (1998)
9. Dryden, I.L., Mardia, K.V.: Statistical shape analysis: with applications in R, vol. 995. Wiley (2016)
10. Eilam-Stock, T., Wu, T., Spagna, A., Egan, L.J., Fan, J.: Neuroanatomical alterations in high-functioning adults with autism spectrum disorder. Front. Neurosci. **10**, 237 (2016)
11. Eltzner, B., Jung, S., Huckemann, S.: Dimension reduction on polyspheres with application to skeletal representations, pp. 22–29. Springer (2015)
12. Feng, Q., Jiang, M., Hannig, J., Marron, J.S.: Angle-based joint and individual variation explained. J. Multivar. Anal. **166**, 241–265 (2018)
13. Fletcher, P.T., Lu, C., Pizer, S.M., Joshi, S.: Principal geodesic analysis for the study of nonlinear statistics of shape. IEEE Trans. Med. Imag. **23**(8), 995–1005 (2004)
14. Gorczowski, K., Styner, M., Jeong, J., Marron, J.S., Piven, J., Hazlett, H.C., Pizer, S.M., Gerig, G.: Statistical shape analysis of multi-object complexes. In: 2007 IEEE Conference on Computer Vision and Pattern Recognition, pp. 1–8 (2007)
15. Gorczowski, K., Styner, M., Jeong, J.Y., Marron, J., Piven, J., Hazlett, H.C., Pizer, S.M., Gerig, G.: Multi-object analysis of volume, pose, and shape using statistical discrimination. IEEE Trans. Pattern Anal. Mach. Intell. **32**(4), 652–661 (2009)
16. Gori, P., Colliot, O., Marrakchi-Kacem, L., Worbe, Y., Poupon, C., Hartmann, A., Ayache, N., Durrleman, S.: A Bayesian framework for joint morphometry of surface and curve meshes in multi-object complexes. Med. Image Anal. **35**, 458–474 (2017)
17. Hong, J.: Classification of neuroanatomical structures based on non-Euclidean geometric object properties. Ph.D. thesis. Computer Science dissertation, University of North Carolina at Chapel Hill (2019)
18. Hong, J., Vicory, J., Schulz, J., Styner, M., Marron, J., Pizer, S.: Non-Euclidean classification of medically imaged objects via s-reps. Med. Image Anal. **31**, 37–45 (2016)
19. Hong, S., Fishbaugh, J., Gerig, G.: 4D continuous medial representation by geodesic shape regression. In: 2018 IEEE 15th International Symposium on Biomedical Imaging (ISBI 2018), pp. 1014–1017. IEEE (2018)
20. Hotelling, H.: Relations between two sets of variates. Biometrika **28**(3–4), 321–377 (1936). https://doi.org/10.1093/biomet/28.3-4.321
21. Huckemann, S., Hotz, T., Munk, A.: Intrinsic shape analysis: Geodesic PCA for Riemannian manifolds modulo isometric Lie group actions. Statistica Sinica pp. 1–58 (2010)
22. Ipsen, I.C., Meyer, C.D.: The angle between complementary subspaces. Am. Math. Mon. **102**(10), 904–911 (1995)
23. Jiang, M.: Statistical learning of integrative analysis. Ph.D. thesis, The University of North Carolina at Chapel Hill (2018)
24. Jung, S., Dryden, I.L., Marron, J.S.: Analysis of principal nested spheres. Biometrika (2012)
25. Katuwal, G.J., Cahill, N.D., Baum, S.A., Michael, A.M.: The predictive power of structural MRI in autism diagnosis. In: 2015 37th Annual International Conference of the IEEE Engineering in Medicine and Biology Society (EMBC), pp. 4270–4273 (2015). https://doi.org/10.1109/EMBC.2015.7319338

26. van der Kloet, F.M., Sebastián-León, P., Conesa, A., Smilde, A.K., Westerhuis, J.A.: Separating common from distinctive variation. BMC Bioinf. **17**(5), 271–286 (2016)

27. Knyazev, A.V., Argentati, M.E.: Majorization for changes in angles between subspaces, ritz values, and graph laplacian spectra. SIAM J. Matrix Anal. Appl. **29**(1), 15–32 (2007)

28. Lindström, A., Pettersson, F., Almqvist, F., Berglund, A., Kihlberg, J., Linusson, A.: Hierarchical pls modeling for predicting the binding of a comprehensive set of structurally diverse protein- ligand complexes. J. Chem. Inf. Model. **46**(3), 1154–1167 (2006)

29. Liu, Z.: Geometric and statistical models for multi-object shape analysis (chapter 2). Ph.D. thesis. Computer Science dissertation, University of North Carolina at Chapel Hill (2022)

30. Liu, Z., Damon, J., Marron, J.S., Pizer, S.: Geometric and statistical models for analysis of two-object complexes. Under review (2022)

31. Liu, Z., Hong, J., Vicory, J., Damon, J.N., Pizer, S.M.: Fitting unbranching skeletal structures to objects. Med. Image Anal. **70**, 102020 (2021)

32. Lock, E.F., Hoadley, K.A., Marron, J.S., Nobel, A.B.: Joint and individual variation explained (JIVE) for integrated analysis of multiple data types. Ann. Appl. Stat. **7**(1), 523 (2013)

33. Marron, J.S., Todd, M.J., Ahn, J.: Distance weighted discrimination. J. Am. Stat. Assoc. **102**(480), 1267–1271 (2007)

34. Miolane, N., Caorsi, M., Lupo, U., Guerard, M., Guigui, N., Mathe, J., Cabanes, Y., Reise, W., Davies, T., Leitão, A., et al.: ICLR 2021 challenge for computational geometry & topology: design and results. arXiv preprint arXiv:2108.09810 (2021)

35. Murphy, C.M., Deeley, Q., Daly, E., Ecker, C., Obrien, F.: Anatomy and aging of the amygdala and hippocampus in autism spectrum disorder: an in vivo magnetic resonance imaging study of asperger syndrome. Autism Res. **5**(1), 3–12 (2012)

36. Nicolson, R., DeVito, T.J., Vidal, C.N., Sui, Y., Hayashi, K.M., Drost, D.J., Williamson, P.C., Rajakumar, N., Toga, A.W., Thompson, P.M.: Detection and mapping of hippocampal abnormalities in autism. Psychiatr. Res. Neuroimaging **148**(1), 11–21 (2006)

37. Pizer, S.M., Hong, J., Vicory, J., Liu, Z., Marron, J.S., et al.: Object shape representation via skeletal models (s-reps) and statistical analysis. Riemannian Geometric Statistics in Medical Image Analysis pp. 233–272 (2019)

38. Pizer, S.M., Jung, S., Goswami, D., Vicory, J., Zhao, X., Chaudhuri, R., Damon, J.N., Huckemann, S., Marron, J.: Nested sphere statistics of skeletal models. In: Innovations for shape analysis, pp. 93–115. Springer (2013)

39. Pizer, S.M., Marron, J., Damon, J., Vicory, J., Krishna, A., Liu, Z., Taheri, M.: Skeletons, object shape, statistics. Front. Comput. Sci. **4**, 842637 (2022)

40. Qiu, A., Adler, M., Crocetti, D., Miller, M.I., Mostofsky, S.H.: Basal ganglia shapes predict social, communication, and motor dysfunctions in boys with autism spectrum disorder. J. Am. Acad. Child Adolesc. Psychiatr. **49**(6), 539–551 (2010)

41. Richards, R., Greimel, E., Kliemann, D., Koerte, I.K., Schulte-Körne, G., Reuter, M., Wachinger, C.: Increased hippocampal shape asymmetry and volumetric ventricular asymmetry in autism spectrum disorder. NeuroImage Clin. **26**, 102207 (2020)

42. Sagonas, C., Panagakis, Y., Leidinger, A., Zafeiriou, S.: Robust joint and individual variance explained. In: Proceedings of the IEEE Conference on Computer Vision and Pattern Recognition, pp. 5267–5276 (2017)

43. Schulz, J., Pizer, S., Marron, J., Godtliebsen, F.: Nonlinear hypothesis testing of geometric object properties of shapes applied to hippocampi. J. Math. Imag. Vis. **54**, 15–34 (2016)

44. Shen, C., Sun, M., Tang, M., Priebe, C.E.: Generalized canonical correlation analysis for classification. J. Multivar. Anal. **130**, 310–322 (2014)

45. Styner, M., Oguz, I., Xu, S., Brechbühler, C., Pantazis, D., Levitt, J., Shenton, M., Gerig, G.: Statistical shape analysis of brain structures using SPHARM-PDM. Insight J. **1071**, 242–250 (2006)

46. Torgerson, W.S.: Multidimensional scaling: I. theory and method. Psychometrika **17**(4), 401–419 (1952)

47. Trygg, J., Wold, S.: O2-PLS, a two-block (X-Y) latent variable regression (LVR) method with an integral OSC filter. J. Chemom. **17**, 53–64 (2003) https://doi.org/10.1002/cem.775

48. Tu, L., Styner, M., Vicory, J., et al.: Skeletal shape correspondence through entropy. IEEE Transactions on Medical Imaging (2018)

49. Van Deun, K., Van Mechelen, I., Thorrez, L., Schouteden, M., De Moor, B., Van Der Werf, M.J., De Lathauwer, L., Smilde, A.K., Kiers, H.A.: Disco-sca and properly applied gsvd as swinging methods to find common and distinctive processes. PLoS One **7**(5), e37840 (2012)

50. Wang, J., Vachet, C., Rumple, A., Gouttard, S., Ouziel, C., Perrot, E., Du, G., Huang, X., Gerig, G., Styner, M.A.: Multi-atlas segmentation of subcortical brain structures via the AutoSeg software pipeline. Front. Neuroinf. **8**, 7 (2014)

51. Wei, S., Lee, C., Wichers, L., Marron, J.: Direction-projection-permutation for high-dimensional hypothesis tests. J. Comput. Graph. Stat. **25**(2), 549–569 (2016)

52. Westerhuis, J.A., Kourti, T., MacGregor, J.F.: Analysis of multiblock and hierarchical PCA and PLS models. J. Chemom. **12**(5), 301–321 (1998)

53. Wold, H.: Partial least squares (2004). https://doi.org/10.1002/0471667196.ess1914

54. Wold, S., Geladi, P., Esbensen, K., Öhman, J.: Multi-way principal components and PLS analysis. J. Chemom. **1**, 41–56 (2005). https://doi.org/10.1002/cem.1180010107

55. Wold, S., Kettaneh, N., Tjessem, K.: Hierarchical multiblock PLS and PC models for easier model interpretation and as an alternative to variable selection. J. Chemom. **10**, 463–482 (1996)

56. Yushkevich, P., Fletcher, P.T., Joshi, S., Thall, A., Pizer, S.M.: Continuous medial representations for geometric object modeling in 2d and 3d. Image Vis. Comput. **21**(1), 17–27 (2003)

Zhiyuan Liu received his Ph.D. from the Department of Computer Science at the University of North Carolina at Chapel Hill (UNC). He was co-advised by Dr. Stephen M. Pizer and Dr. J. S. Marron. His research interest lies in analyzing complex data such as shape data and graph data.

Jörn Schulz studied mathematics at the Humboldt University of Berlin, Germany. He received his Ph.D. from the Arctic University of Norway in 2013 with a thesis in statistical analysis of medical shapes and directional data. He is currently an Associate Professor of Mathematics and Physics at the University of Stavanger (UiS), Norway.
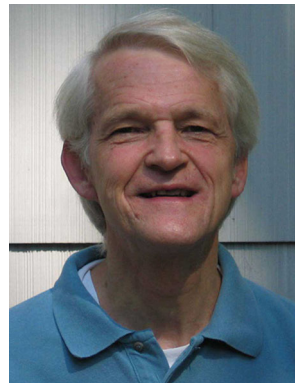
James Damon is an emeritus professor in the Mathematics Department at UNC. He received the B. A. degree in mathematics from Dartmouth College in 1967, and the Ph. D. from the Harvard University in 1972.

Mohsen Taheri studied applied mathematics in Iran, Azad University of Tehran. He received the Master's degree in mathematics and physics from the University of Stavanger (UiS) in Norway with a thesis in statistical shape analysis of brain structures. Currently, He is a Ph.D. student in medical statistics and a member of biomedical data analysis laboratory (BMDLab) at UiS.

Stephen Pizer is a Kenan Professor of Computer Science, Radiation Oncology, Radiology, and Biomedical Engineering at UNC. He received the Bachelor degree in applied mathematics from Brown University in 1963 and the Ph.D. in computer science from Harvard in 1967. He founded and has led UNC's multidepartmental MIDAG. He is Fellow of the MICCAI Society. For many years he was Associate Editor of IEEE Transactions on Medical Imaging.

Martin Styner is a research associate professor in the Department of Computer Science with a joint appointment as an assistant professor in the Department of Psychiatry at UNC. He is the co-director of the UNC Neuro Image Research and Analysis Laboratory and associate director of the Developmental Neuroimaging Core in the Carolina Institute for Developmental Disabilities at UNC.

J. S. Marron is the Amos Hawley Distinguished Professor of Statistics and Operations Research at UNC. He received the B. S. degree from the University of California at Davis, and the Ph.D. from the University of California at Los Angeles. Marron has held the positions of Assistant, Associate and Full Professor with UNC, and is also Adjunct Professor of Computer Science and Member of the Lineberger Comprehensive Cancer Center.